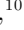# Worlds Next Door: A Candidate Giant Planet Imaged in the Habitable Zone of α Cen A.
I. Observations, Orbital and Physical Properties, and Exozodi Upper Limits

Charles Beichman [1,2,*], Aniket Sanghi [3,4,*], Dimitri Mawet [3,2], Pierre Kervella [5,6], Kevin Wagner [7],
Billy Quarles [8], Jack J. Lissauer [9], Max Sommer [10], Mark Wyatt [10], Nicolas Godoy [11],
William O. Balmer [12,13], Laurent Pueyo [13], Jorge Llop-Sayson [2], Jonathan Aguilar [13],
Rachel Akeson [1], Ruslan Belikov [9], Anthony Boccaletti [5], Elodie Choquet [11], Edward Fomalont [14,15],
Thomas Henning [16], Dean Hines [13], Renyu Hu [2], Pierre-Olivier Lagage [17], Jarron Leisenring [18],
James Mang [19,4], Michael Ressler [2], Eugene Serabyn [2], Pascal Tremblin [20], Marie Ygouf [2] and
Mantas Zilinskas [2]

[1] NASA Exoplanet Science Institute, Caltech-IPAC, Pasadena, CA 91125, USA
[2] Jet Propulsion Laboratory, California Institute of Technology, Pasadena, CA 91109, USA
[3] Cahill Center for Astronomy and Astrophysics, California Institute of Technology, 1200 E. California Boulevard, MC 249-17, Pasadena, CA 91125, USA
[4] NSF Graduate Research Fellow
[5] LIRA, Observatoire de Paris, Université PSL, Sorbonne Université, Université Paris Cité, CY Cergy Paris Université, CNRS, 5 place Jules Janssen, 92195 Meudon, France
[6] French-Chilean Laboratory for Astronomy, IRL 3386, CNRS and U. de Chile, Casilla 36-D, Santiago, Chile
[7] Department of Astronomy and Steward Observatory, University of Arizona, USA
[8] Department of Physics and Astronomy, East Texas A&M University Commerce, TX 75428, USA
[9] Space Science & Astrobiology Division, Building 245, NASA Ames Research Center, Moffett Field, CA 94035, USA
[10] Institute of Astronomy, University of Cambridge, Madingley Road, Cambridge CB3 0HA, UK
[11] Aix Marseille Univ., CNRS, CNES, LAM, Marseille, France
[12] Department of Physics & Astronomy, Johns Hopkins University, 3400 N. Charles Street, Baltimore, MD 21218, USA
[13] Space Telescope Science Institute, 3700 San Martin Drive, Baltimore, MD 21218, USA
[14] National Radio Astronomy Observatory, 520 Edgemont Rd., Charlottesville, VA 22903, USA
[15] ALMA, Vitacura, Santiago, Chile
[16] Max-Planck-Institut für Astronomie (MPIA), Königstuhl 17, 69117 Heidelberg, Germany
[17] Université Paris-Saclay, Université Paris Cité, CEA, CNRS, AIM, 91191 Gif-sur-Yvette, France
[18] Steward Observatory, University of Arizona, Tucson, AZ 85721, USA
[19] Department of Astronomy, University of Texas at Austin, Austin, TX 78712, USA
[20] Université Paris-Saclay, UVSQ, CNRS, CEA, Maison de la Simulation, 91191 Gif-sur-Yvette, France

ABSTRACT

We report on coronagraphic observations of the nearest solar-type star, α Cen A, using the MIRI instrument on the *James Webb* Space Telescope. The proximity of α Cen (1.33 pc) means that the star's habitable zone is spatially resolved at mid-infrared wavelengths, so sufficiently large planets or quantities of exozodiacal dust would be detectable via direct imaging. With three epochs of observation (August 2024, February 2025, and April 2025), we achieve a sensitivity sufficient to detect $T_{\rm eff} \approx$ 225–250 K (1–1.2 $R_{\rm Jup}$) planets between $1''$–$2''$ and exozodiacal dust emission at the level of $>$5–8× the brightness of our own zodiacal cloud. The lack of exozodiacal dust emission sets an unprecedented limit of a few times the brightness of our own zodiacal cloud—a factor of $\gtrsim$ 10 more sensitive than measured toward any other stellar system to date. In August 2024, we detected a $F_\nu(15.5~\mu m) =$ 3.5 mJy point source, called $S1$, at a separation of $1.5''$ from α Cen A at a contrast level of 5.5×10^{-5}. Because the August 2024 epoch had only one successful observation at a single roll angle, it is not possible to unambiguously confirm $S1$ as a bona fide planet. Our analysis confirms that $S1$ is neither a background nor a foreground object. $S1$ is not recovered in the February and April 2025 epochs. However, if $S1$ is the counterpart of the object, $C1$, seen by the VLT/NEAR program in 2019, we find that there is a 52% chance that the $S1 + C1$ candidate was missed in both follow-up JWST/MIRI

Corresponding author: Charles Beichman & Aniket Sanghi

Email: chas@ipac.caltech.edu, asanghi@caltech.edu

observations due to orbital motion. Incorporating constraints from the non-detections, we obtain families of dynamically stable orbits for $S1 + C1$ with periods between 2–3 years. These suggest that the planet candidate is on an eccentric ($e \approx 0.4$) orbit significantly inclined with respect to the α Cen AB orbital plane ($i_{\mathrm{mutual}} \approx 50°$, prograde, or $\approx 130°$, retrograde). Based on the photometry and inferred orbital properties, the planet candidate could have a temperature of 225 K, a radius of $\approx$1–1.1 R_{Jup} and a mass between 90–150 $M_{\oplus}$, consistent with RV limits. This paper is first in a series of two papers: Paper II (Sanghi & Beichman et al. 2025, in press) discusses the data reduction strategy and finds that $S1$ is robust as a planet candidate, as opposed to an image or detector artifact.

1. INTRODUCTION

α Centauri A is the closest solar-type star to the Sun and offers a unique opportunity for direct imaging with the *James Webb* Space Telescope (JWST) to detect an exoplanet within its habitable zone and to achieve an unprecedented level of sensitivity for the detection of an exozodiacal dust cloud (Beichman et al. 2020; Sanghi et al. 2025). Among the nearby stars, α Cen A, *primus inter pares*, offers a nearly 3-fold improvement in the angular scale of its Habitable Zone and a 7.5-fold boost in the absolute brightness of any planet compared to the next nearest solar type star, τ Ceti. Specifically, the F1550C coronagraph onboard the Mid-InfraRed Instrument (MIRI) can be used to probe the 1–3 au ($<4''$) region around α Cen A which is predicted to be stable within the α Cen AB system for exoplanets and/or an exozodiacal dust cloud (Quarles, Lissauer & Kaib 2018; Cuello & Sucerquia 2024). The detection of a planet or exozodiacal emission, or more stringent limits on either, would advance our understanding of the formation of planetary systems in binary stellar systems and yield an important target for future observations with both JWST and the extremely large ground-based telescopes. Of particular interest is the ability of JWST/MIRI to confirm the detection of a candidate ($C1$) identified using the VISIR mid-infrared camera (10–12.5 μm) on ESO's Very Large Telescope (VLT) as part of the NEAR (New Earths in Alpha Centauri Region) Breakthrough Watch Project (Wagner et al. 2021).

In this paper, we present the results of a deep search for planets and zodiacal dust emission obtained with three epochs of JWST/MIRI coronagraphic imaging observations of α Cen A. This paper is the first in a series and is followed by Sanghi & Beichman et al. (2025, also referred to as Paper II). It is organized as follows. Section 2 describes the observational strategy and program execution. Section 3 summarizes key aspects of the data processing strategy, the detection of a candidate exoplanet in the August 2024 data, the planet temperature sensitivity of our observations, and upper lim-

its on the presence of exozodiacal emission. Section 4 analyzes possible orbital configurations for the candidate planet. The planet's physical properties, as constrained by its observed brightness and orbit, as well as by radial velocity measurements (Wittenmyer et al. 2016; Zhao et al. 2018), are considered in Section 5. Section 6 discusses the importance of the presence of the candidate planet and the upper limits on exozodiacal emission in the context of theories of planet and disk formation in binary systems, as well as prospects for recovering the candidate in future observations. Finally, Section 7 presents our conclusions. Appendix A provides the complete details of observation preparation and Appendix B includes new ALMA astrometry and an updated ephemeris for the α Cen AB system.

2. OBSERVATIONS

2.1. *Observational Strategy*

We elected to observe with MIRI and its Four Quadrant Phase Mask Coronagraph (4QPM; Rieke et al. 2015; Wright et al. 2015; Boccaletti et al. 2022) centered at 15.5 μm (the F1550C filter) for a number of reasons: (1) favorable star-planet contrast ratio for the 200–350 K temperatures expected for a planet heated by α Cen A at 1–3 au; (2) low susceptibility to the effects of wavefront drift at this long wavelength; and (3) the reduced brightness of background objects with typical stellar photospheres. However, despite these advantages, the α Cen AB system presents numerous challenges in planning and executing coronagraphic measurements with JWST at any wavelength.

- The presence of α Cen B only $7''$–$9''$ away from α Cen A puts the full intensity of this bright, [F1550C] ~ -0.59 mag star in the focal plane at a position that cannot be attenuated. We developed a strategy (§A.4) to place ϵ Mus at the position α Cen B would occupy (unocculted) during the observation of α Cen A (occulted). This observation would provide a PSF reference to mitigate the effects of α Cen B.

- The selection of a reference star is complicated by the requirement that it be both comparably bright

Table 1. Stellar Properties

Property	α Cen A	α Cen B	ϵ Mus	References
Spectral Type	G2V	K1V	M4III	1, 2
Mass ($M_\odot$)	1.0788 ± 0.0029	0.9092 ± 0.0025	$\cdots$	3
Luminosity ($L_\odot$)	1.5059 ± 0.0019	0.4981 ± 0.0007	$\cdots$	3
K (mag)	-1.48 ± 0.05	-0.60 ± 0.05	-1.42 ± 0.05	2, 4
F1065C	-1.51 ± 0.05 (160 Jy)	-0.59 ± 0.05 (51 Jy)	-1.9 ± 0.1 (194 Jy)	5, 6, 7
F1140C	-1.51 ± 0.05 (120 Jy)	-0.59 ± 0.05 (59 Jy)	-1.9 ± 0.1 (180 Jy)	5, 6, 7
F1550C	-1.51 ± 0.05 (63 Jy)	-0.59 ± 0.05 (28 Jy)	-2.0 ± 0.1 (100 Jy)	5, 6, 7
Parallax (mas)	750.81 ± 0.38		9.99 ± 0.20	3, 8
Distance (pc)	1.33		100	3, 8
Proper Motion (μ_α, μ_δ, mas yr^{-1})	$(-3639.95 \pm 0.42, +700.40 \pm 0.17$)		$(-231.04 \pm 0.19, -26.39 \pm 0.26)$	3, 8
R.A.	14:39:26.155	14:39:25.9421	12:17:33.620	3, 8, 9
Decl.	-60:49:56.287	-60:49:51.334	-67:57:39.072	3, 8, 9

References—(1) Valenti & Fischer (2005); (2) Ducati (2002); (3) Akeson et al. (2021); (4) Engels et al. (1981); (5) from angular size of α Cen A, Θ = 8.502 mas combined with a Kurucz-Castelli model with $T_{\rm eff}$ = 5795 K and log g = 4.312 dex (cgs units; Kervella et al. 2017); (6) From fit to Kurucz model atmosphere using VOSA SED utility (Engels et al. 1981; Ducati 2002; Castelli & Kurucz 2003; Bayo et al. 2008); (7) Olnon et al. (1986); (8) Gaia Collaboration et al. (2016); (9) for ϵ Mus Epoch 2016.0 (Gaia DR3) and for α Cen Epoch 2019.5 (Akeson et al. 2021).

to α Cen A and have similar photospheric properties in the F1550C waveband.

- The moment-by-moment position of α Cen A is the result of a complex interplay of its high proper motion and parallax (as calculated for the location of JWST at the epoch of observation), and of the orbital motion of α Cen A and α Cen B about their common center of mass (see Akeson et al. 2021, and Table 1).

- With [F1550C] ~ -1.5 mag, α Cen A is too bright for direct target acquisition (TA) with MIRI, necessitating a blind offset from a nearby star with an accuracy of <10 mas to avoid degradation of the coronagraphic contrast (Boccaletti et al. 2015). The chosen reference star ϵ Mus (§A.1) is similarly too bright for direct TA, also necessitating a blind offset.

- Offset stars must be of sufficient astrometric accuracy, be as close as possible to α Cen A or ϵ Mus, but not affected by diffraction or other artifacts from the target stars, and be of sufficient brightness to be readily detectable in a short TA observation at F1000W (Figure 1).

- The time of observation should minimize the change in solar aspect angle between target and reference star observations and thus minimize the change in the telescope's thermal environment.

- Finally, all MIRI coronagraphic observations using the 4QPM are affected by excess background radiation appearing around the quadrant boundaries referred to as the "Glow Sticks" (Boccaletti et al. 2022).

2.2. Planned Observation Sequences

The above considerations led to the observational sequences described below and detailed in Appendix A. Based on in-flight performance, JWST can place both the target and reference star with an accuracy of ∼5–7 mas (1σ, each axis) behind the MIRI/4QPM. To provide diversity in determining the PSF for post-processing, we selected a 9-point dither pattern for observing the reference star. The multiple reference PSF observations improve the ability of post-processing algorithms to remove residual stellar speckles and help to mitigate wavefront error (WFE) drifts over the 32 hr duration of the entire sequence. The measurement strategy was as follows:

1. Offset from a Gaia star (G9 in Figure 1) to place ϵ Mus at the center of the F1550C coronagraphic mask and make a 9-point dithered set of image observations of the reference star behind the MIRI/4QPM. This is followed by observations of a background field to subtract the Glow Stick.

2. Place ϵ Mus at the detector location that α Cen B would occupy in the Roll #1 observation to help
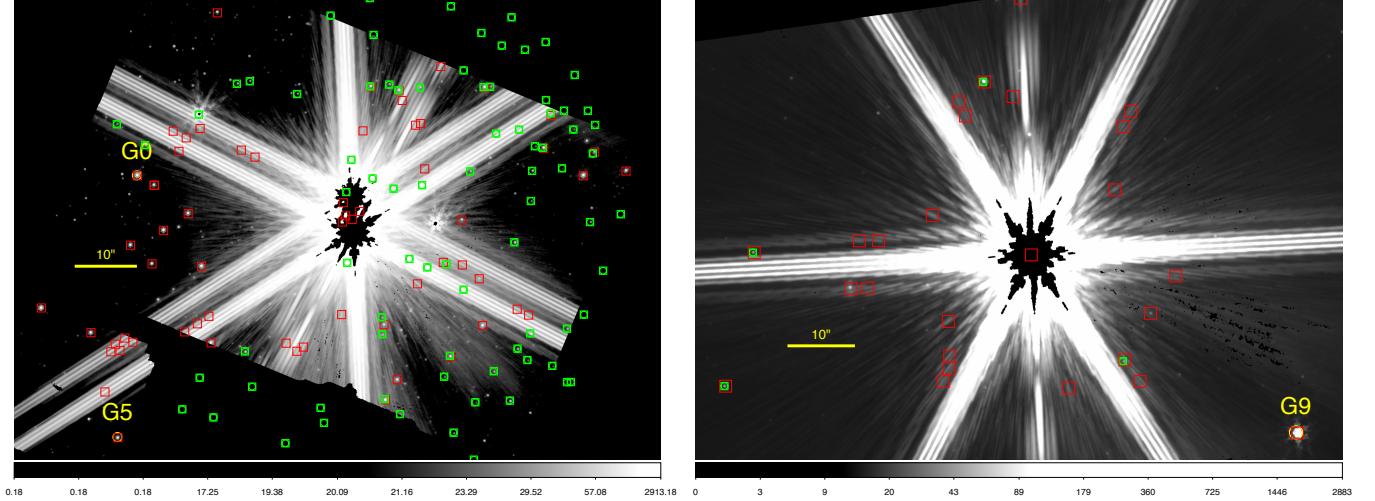
Figure 1. *Left:* F1000W image of α Cen AB showing Gaia stars (green boxes) and MIRI detections (red boxes). The stars labeled $G0$ and $G5$ were used for target acquisition of α Cen A. *Right:* similar F1000W image for ϵ Mus. The star labeled $G9$ was used for target acquisition of ϵ Mus.

mitigate speckles from the unocculted star at the position of α Cen A.

3. Offset from a Gaia star ($G0$ or $G5$ in Figure 1) to place α Cen A at the center of the F1550C coronagraphic mask at the Roll #1 V3PA[1] angle for a sequence of 1250 images, followed by observations of a background field to subtract the Glow Stick.

4. Repeat the α Cen A sequence (#3) at a second V3PA angle (Roll #2).

5. Repeat the ϵ Mus 9-point dither sequence (#1) at the mask center.

6. Repeat the off-axis ϵ Mus observation sequence (#2) but at the detector position of α Cen B in the Roll #2 observation.

2.3. *Executed Observation Sequences*

The observations of α Cen A (Cycle 1 GO, PID #1618; PI: Beichman, Co-PI: Mawet) were initiated in August 2023, but were unsuccessful due to target acquisition and offset failures. A sequence of short test images was obtained in June and July 2024 to validate the target acquisition strategy. Specifically, in July 2024, we executed #1 without dithering and #3 with fewer integrations.[2] Following successful execution of the test pro-

gram, we conducted our full-set of science observations in August 2024. We successfully executed steps #1, #4, and #6 (#2 was not part of the sequence planned for this observation). However, the first roll on α Cen A (#3) and the second ϵ Mus observation (#5) were unsuccessful due to guide star failures.

Based on results from the August 2024 data, the STScI Director's Office approved a follow-up Director's Discretionary Time (DDT) program (PID #6797; PI: Beichman, Co-PI: Sanghi). The complete two roll sequence with associated reference star observations (#1–#6) was attempted in February 2025 as part of this DDT program, but due to a telescope pointing anomaly, the first α Cen A roll (#3) was not executed. All other observations were successful.

The STScI Director's Office approved a second follow-up DDT program (PID #9252; PI: Beichman, Co-PI: Sanghi), which resulted in the successful execution of a full two roll sequence in April 2025. A summary log of all successful observations is provided in Table A3. In all cases, the accuracy of the offsets from Gaia stars was consistent with the expected initial pointing accuracy (1σ, 5–7 mas), the offset accuracy (1σ, 1.5 mas) and the line-of-sight jitter (1σ, 1.5 mas) during the observing sequence at each position. The February 2025 Roll 2 and April 2025 Roll 1 observations showed offsets of > 10 mas from the 4QPM center or from the Eps Mus dither pattern and were thus of lower quality (see dither map in Sanghi & Beichman et al. 2025).

---

[1] V3PA is the position angle (PA) of the V3 reference axis eastward relative to north when projected onto the sky.

[2] No ϵ Mus reference star observation was acquired at the detector position of α Cen B in the July 2024 test observations. This severely compromised the quality of PSF subtraction. Hence, these observations are not presented.

JWST/MIRI F1550C Observations of α Centauri AB
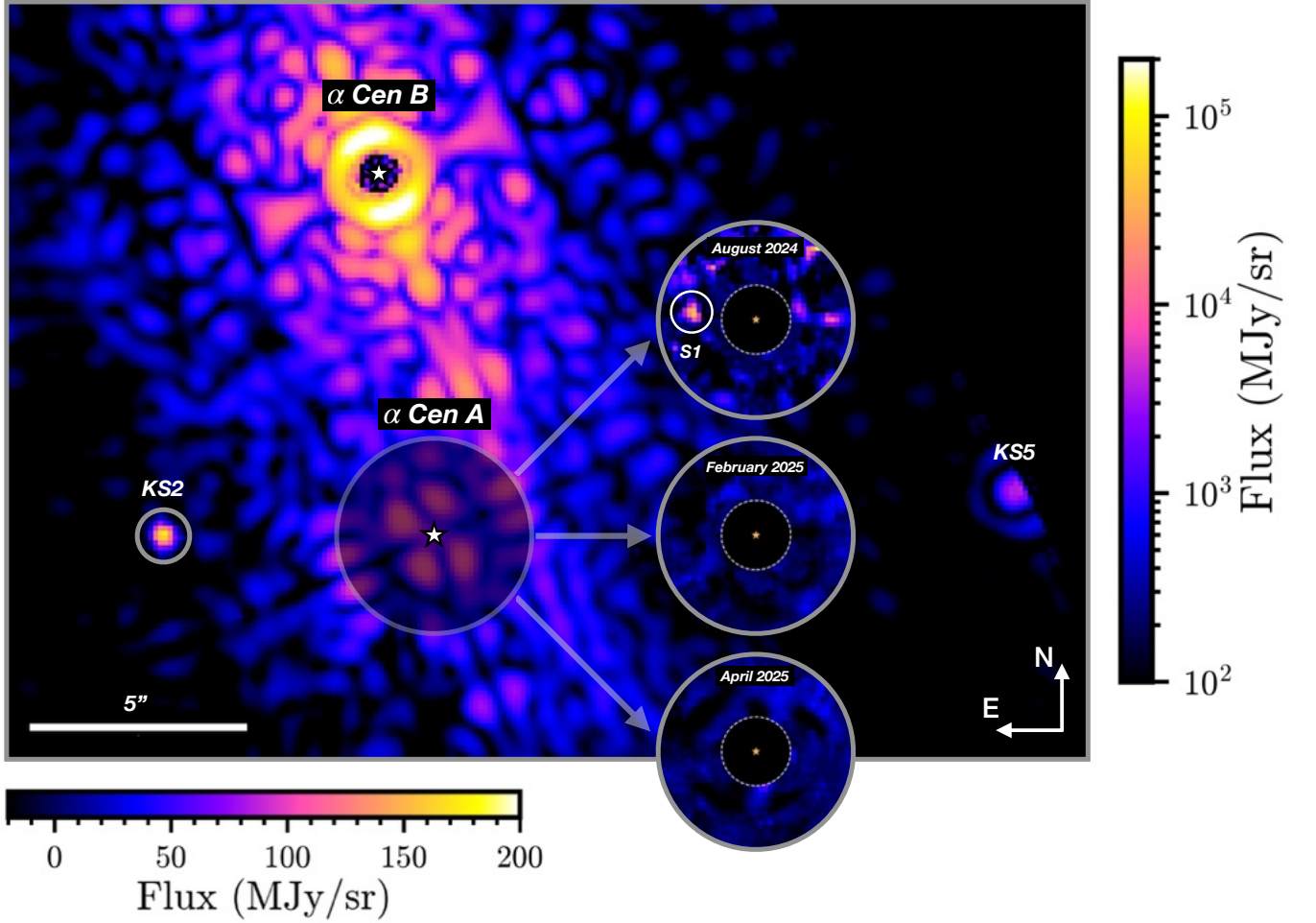
Figure 2. JWST's view of the α Cen AB system. Shown above is a background-subtracted Stage 2b F1550C image of the α Cen AB system from August 2024. The image is oriented North up and East left. The white stars denote the approximate positions of α Cen B, saturated near the top of the image, and α Cen A in the lower part of the image hidden behind the F1550C mask. The right colorbar (logarithmically scaled) is associated with this image. At the edge of the detector, to the West of α Cen A, is a known background source KS5 (Kervella et al. 2016). To the East of α Cen A is known background source KS2 (Kervella et al. 2016), shown as an inset, as it is only detected after performing PSF subtraction (no colorbar shown for the inset, scaled linearly between −5 and 50 MJy/sr). An ≈2″75 radius region around α Cen A is shaded and mapped to three PSF-subtracted images, one for each observation epoch. Candidate $S1$ is seen only in August 2024. The bottom colorbar (linearly scaled) is associated with the three PSF-subtracted images. For reference, 1 MJy/sr ≈ 4.6×10^{-6} Jy/AiryCore, where AiryCore is defined as the area of a circular aperture of diameter 1 FWHM (≈ 0″5).

3. RESULTS

3.1. *Summary of Data Reduction*

Paper II (Sanghi & Beichman et al. 2025) describes in detail the initial pipeline processing, PSF subtraction techniques for both α Cen A and α Cen B, source identification steps, the photometry and astrometry estimation procedures, and detection sensitivity analysis. Here, we provide a short summary. Level 0 data products were downloaded from MAST, processed for best up-the-ramp calculation of source brightness and bad pixel rejection (Brandt 2024; Carter et al. 2025), and post-processed to remove the residual stellar diffraction from α Cen A and α Cen B. We assembled distinct reference PSF libraries for each epoch consisting of the individual 400 frames (per dither position) of each 9-pt SGD observation of ε Mus behind the 4QPM and the individual 1250 frames of ε Mus at the unocculted position of α Cen B (for a given roll) obtained at the corresponding epoch. We employed reference star differential imaging (RDI) and jointly subtracted α Cen AB from the 1250 α Cen integrations using the principal component analysis-based Karhunen-Loève Image Processing

Table 2. Observations of a Candidate Planet Orbiting α Cen A

ID	Epoch	$(\Delta\alpha, \Delta\delta)$ ($''$)	(ρ, θ) ($''$, °)	Wavelength (μm)	Flux (mJy)	Contrast to α Cen A	S/N
$C1$	June 1, 2019	$(-0.64, -0.56) \pm 0.05$	$(0.85 \pm 0.05, 228.9 \pm 3.3)$	11.25	1.2 ± 0.4	0.8×10^{-5}	3
$S1$	August 10, 2024	$(1.50, 0.17) \pm 0.13$	$(1.51 \pm 0.13, 83.5 \pm 4.9)$	15.5	3.5 ± 1.0	5.5×10^{-5}	4–6

Note—Observations of $C1$ were obtained in 2019 by the VLT/NEAR experiment Wagner et al. (2021). Position angle (θ) is measured East of North.

algorithm (Soummer et al. 2012). Signal-to-noise ratio maps were generated to search for point sources (Mawet et al. 2014) and extended emission (custom method), and assess detection significance.

3.2. Detection of a Point Source Around α Cen A

A comprehensive search of the $\sim 3''$ region around α Cen A revealed a single point-like source in the August 2024 data, $S1$ (Figure 2). The source was detected $\approx 1\!''\!.5$ East of α Cen A at a S/N between 4–6 (corresponding to a 3.3–4.3σ Gaussian significance for the equivalent false positive probability, see Paper II) with a flux density of ≈ 3.5 mJy (Table 2). The contrast of $S1$ with respect to α Cen A in the F1550C bandpass is $\approx 5.5 \times 10^{-5}$. $S1$ is not recovered in the February and April 2025 observations (Figure 2). At wider separations, in all three epochs, we identified two objects denoted KS2 and KS5 that are known from deep 2 μm VLT/NACO imaging to be background stars (Kervella et al. 2016). In the August 2024 data, KS2 is seen $\approx 6''$ East of α Cen A, after post-processing, exactly in the position expected for a distant, low proper motion star (Figure 2). The bright object KS5 ($K_s \sim 7$ mag) is detected just off the edge of the coronagraphic field and will eventually pass within a few mas of α Cen A (mid-2028; Kervella et al. 2016).

Paper II (Sanghi & Beichman et al. 2025) discusses the robustness of the detection of $S1$ and with the help of several tests, presents reasonable evidence that $S1$ is a celestial signal, as opposed to an image artifact. Three primary artifact scenarios are shown to be unlikely:

- $S1$ *is not likely a short-lived detector artifact in the α Cen AB integrations.* $S1$ was independently detected in multiple subsets of the full 1250 frame integration sequence (Section 4.2.3, Paper II). Additionally, there was no evidence for transient "hot pixels" in the data, centered on $S1$.

- $S1$ *is not likely a PSF-subtraction artifact from the ϵ Mus coronagraphic reference images.* $S1$ was detected in post-processing analyses performed by iteratively excluding each one of the nine dither positions ("leave-one-out" analysis, Section 4.2.4, Paper II).

- $S1$ *is not likely a PSF-subtraction artifact from imperfect subtraction of α Cen B.* $S1$ is well matched to the expected PSF profile and behaves differently with respect to changes in subtraction parameters from another point-like object ($A1$) identified as an artifact from α Cen B. $A1$'s signal disappears both when the number of azimuthal subsections and number of principal components increases. $S1$'s signal persists in both cases (Section 4.2.2, Paper II).

To assess whether $S1$ is physically associated with α Cen A, we address whether it could be either a background or foreground (Solar System) object. Multiple arguments rule out these scenarios:

- First and most conclusively, the JWST data themselves provide definitive evidence against the hypothesis that $S1$ is a background object. No point source counterparts to $S1$ are detected at the expected location for a background source in the February 2025 and April 2025 observations (Figure 3). See Paper II (Sanghi & Beichman et al. 2025) for further details.

- Archival images taken by Spitzer/IRAC (Rieke & Gautier 2004), 2MASS, and VLT/NACO (Kervella et al. 2016) when α Cen A was up to one arcminute away from its current position do not show any sources at the $S1$ position. We also considered the effects of interstellar extinction on background source detectability in archival imaging. Extinction maps from Planck and stellar data along the line-of-sight toward α Cen provide a range $20 < A_V(\text{mag}) < 40$ (Planck Collaboration et al. 2016; Zhang & Kainulainen 2022), making more extreme A_V values unlikely.[3] As

---

[3] Planck Extinction maps:
https://irsa.ipac.caltech.edu/data/Planck/release_2/all-sky-maps/maps/component-maps/foregrounds/COM_CompMap_Dust-DL07-AvMaps_2048_R2.00.fits
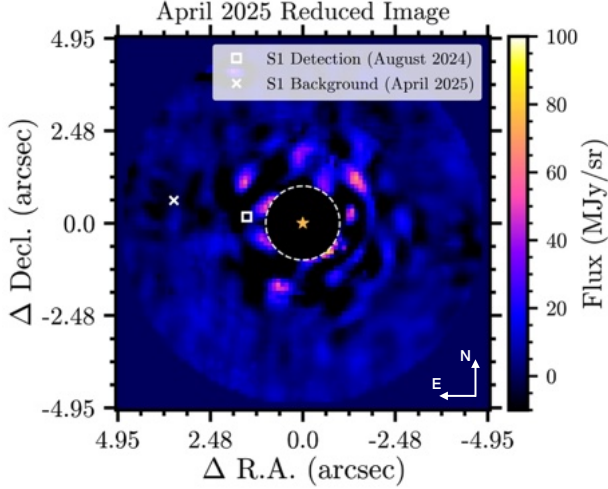
Figure 3. PSF-subtracted image centered on α Cen A for the April 2025 observations, which provides the longest time-baseline to test the stationary background source hypothesis. A square marks the location where $S1$ was detected in the August 2024 epoch. A cross marks the expected location of $S1$ if it were a fixed background object and showed apparent motion with respect to α Cen A due to the star's parallactic and proper motion. No source is detected at this location.

shown in Figure 4, if $S1$ were a reddened star (an M0III Kurucz model with $T_{\mathrm{eff}} = 3800$ K is shown; Buser & Kurucz 1992) or a normal star-dominated galaxy, its emission would be 4 to 25 times brighter at IRAC wavelengths than at F1550C and would have been detectable by Spitzer, or in the deep NACO K-band image. This argument applies to any stellar temperature, since at these wavelengths the emission is approximately Rayleigh-Jeans.

- Figure 4 also shows the spectral energy distribution for a non-photosphere dominated galaxy, the prototypical starburst galaxy or ULIRG, Arp 220, at zero redshift (Polletta et al. 2007). Such an object could have escaped detection in the archival datasets, but the probability of chance alignment with an extragalactic background object is extremely low based on source-counting studies in the MIRI broadband filters. Stone et al. (2024) find that the background density of $F_\nu(F1500W) \gtrsim 1$ mJy sources is <0.05 arcmin^{-2}, corresponding to a chance alignment likelihood $< 4 \times 10^{-4}$ within a $3''$ field-of-view.

- We eliminate the possibility that $S1$ is a foreground Solar System object in a number of ways. An inner main belt asteroid (MBA) at 2.2 AU with a typical temperature of 200 K would have to have a diameter of > 2 km to emit ~ 3 mJy at 15.5 μm.
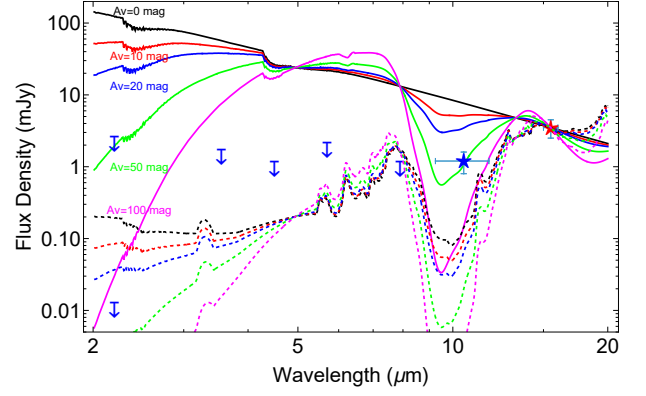

Figure 4. Limits from archival imaging at $S1$'s position. The solid, color-coded lines show a photospheric model for an M0III star ($T_{\mathrm{eff}} = 3800$ K) reddened by increasing levels of extinction, all normalized to 3.5 mJy at 15.5 μm (red star). The blue star denotes the flux density of the object denoted $C1$ detected by the VLT/NEAR experiment (Wagner et al. 2021). The dashed lines show the spectral energy distribution of a typical star-burst galaxy or ULIRG (Arp 220) similarly reddened. Upper limits at the position of $S1$ come from observations at earlier epochs with Spitzer/IRAC (3–8 μm), 2MASS, and NACO (Kervella et al. 2016).

Such objects are extremely rare, $< 10^{-4}$ brighter than 3 mJy at 12 μm in a $5' \times 5'$ field at α Cen A's ecliptic latitude of $\beta = -42°$ (Brooke 2003). Furthermore, the completeness for such large MBAs is over 90% and the Minor Planet Catalog shows no known objects at the position of α Cen A at the August epoch[4]. Finally, as described in Paper II, there is no angular motion seen between the beginning and the end of ~ 2.5 hour MIRI observation compared to the expected >10 arcsec/hr motion for an MBA at the solar elongation of our observations, $\approx 100°$ (Brooke 2003).

Based on all of the above considerations, we pursue the hypothesis that $S1$ is a planet physically associated with and in orbit around α Cen A, as opposed to an artifact or an astrophysical contaminant, and investigate its properties. Given that $S1$ is only detected in a single roll observation in August 2024, we emphasize that it is, at the moment, a *planet candidate*. Additional sightings of $S1$ are required with JWST, or other upcoming facilities, to confirm what would be "α Cen Ab".

---

[4] https://minorplanetcenter.net/cgi-bin/checkmp.cgi
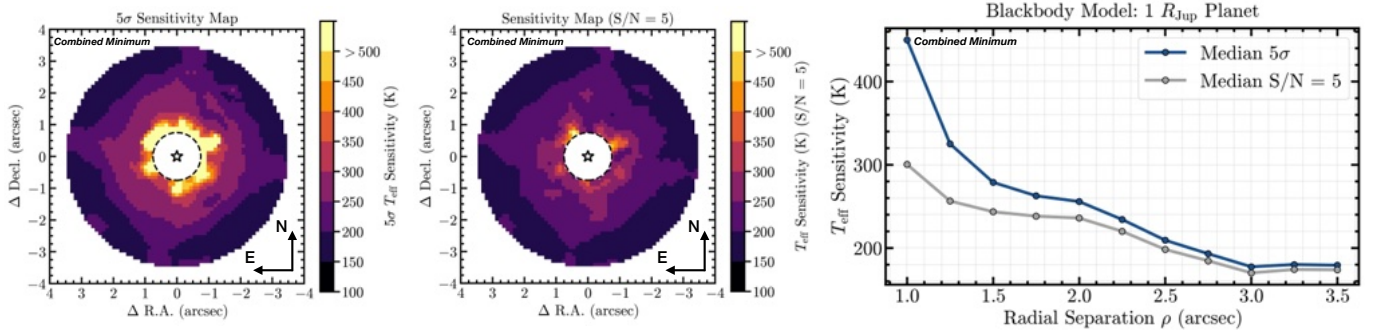
Figure 5. *Left:* two-dimensional 5σ planet effective blackbody temperature sensitivity map, combined across all epochs by selecting the best sensitivity ("combined minimum", see Paper II), in sky coordinates (North up, East left). The central region ($< 0\rlap{.}''75$, or < 1.5 FWHM, radial separations) is masked (poor detectability). A discrete colormap is chosen to highlight the different sensitivity zones across the image. *Center:* same as the left panel for a $S/N = 5$ detection threshold. *Right:* 5σ and $S/N = 5$ median planet effective blackbody temperature curves combined across all epochs.

3.3. *Planet Detection Limits with JWST/MIRI*

We assess our sensitivity to planets around α Cen A across all three epochs of MIRI F1550C observations. Paper II (Sanghi & Beichman et al. 2025) presented the calculation of 2D flux/contrast sensitivity maps. Here, we use the "combined minimum" map from Paper II, which corresponds to the 2D sensitivity map with the best flux sensitivity across all three epochs at each location where the PSF injection-recovery test was performed. We convert the 5σ and $S/N = 5$ flux sensitivities (see Paper II) to effective temperatures (T_{eff}) assuming a blackbody model and a typical planet radius of 1 R_{Jup} (for smaller planets, the minimum detectable planet T_{eff} increases). The results are shown in Figure 5. The MIRI F1550C observations are sensitive to $T_{\mathrm{eff}} \approx 250$ K (1 R_{Jup}) planets between $1''$–$2''$ for a $S/N = 5$ detection threshold. Planets colder than 200 K can be detected at wider separations ($> 2\rlap{.}''5$). We note here that more realistic planet atmospheric models may have a higher brightness temperature (and thus flux) in the F1550C bandpass relative to the effective blackbody temperature assumed here (see §5.2, for example). This would improve the detectability of colder planets at smaller separations than presented here.

### 3.4. *Limits on Extended Emission around α Cen A*

Beichman et al. (2020) predicted that JWST's ability to resolve the habitable zone around α Cen A would result in unprecedented sensitivity to warm dust—the analog of the thermal emission from dust generated by collisions the asteroid belt in our solar system. We show below that the current observations have not only met but exceeded those expectations with limits as low as a few times the solar system brightness levels at 15.5 μm.

3.4.1. *Exozodi Model Description*

As described in Paper II, we injected a number exozodiacal cloud models into the processed α Cen datacubes to set limits on extended "exozodiacal" emission around α Cen A. In the case of α Cen A, stable orbits—and thus significant dust buildup—are limited to within the stable zone, approximately <3 au from the star. The Solar System zodiacal cloud is therefore a poor proxy for a potential exozodi around α Cen A. For a more realistic representation, we consider the scenario of an asteroid belt analogue (ABA) located between 2–3 au, where dust is produced in collisions, which is then transported inward under Poynting-Robertson (PR) drag. This scenario is captured by the semi-analytical model of Rigley & Wyatt (2020), which combines approaches to determine (1) the size distribution arising in a planetesimal belt under collisions and PR drag loss (Wyatt et al. 2011), and (2) how it evolves interior to the belt under further collisional and drag-induced evolution (Wyatt 2005). The resulting optical depth distribution (across grain sizes and disk radii) is then combined with the particles' thermal emission properties, determined using Mie theory, to compute the disk's surface brightness distribution.

Following the approach of Sommer et al. (2025), we generate astrophysical scenes of the inclined, edge-on disks from the respective surface brightness profiles, and convolve them with the spatially varying PSF of the F1550C coronagraphic filter (modeled using STPSF, Perrin et al. 2014), before injecting them into the MIRI datacubes. An example of an exozodi scene, before and after PSF convolution, alongside a PSF subtracted image obtained after model injection, is shown in Figure 6. Note that all exozodiacal disks considered here are assumed to be coplanar with the α Cen AB plane, which is a reasonable assumption for potential circumstellar
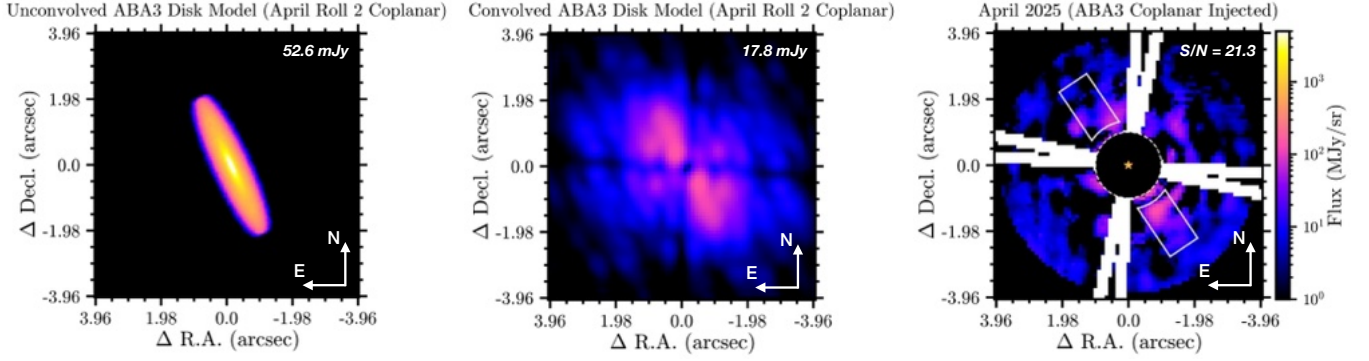
Figure 6. *Left:* unconvolved asteroid belt analogue-3 (ABA-3) exozodi model coplanar with the α Cen AB binary. *Center:* the exozodi model in the left panel after PSF convolution (for the April 2025 observation orientation). *Right:* PSF-subtracted image showing the recovery of the ABA 3 exozodi model injected in the raw α Cen AB dataset from the April 2025 observations. The regions of the image affected by the MIRI 4QPM transition boundaries at each roll are masked. The aperture that yielded the highest S/N (= 21.3) detection for the injected disk is shown (see Paper II for details). All images are plotted on a common logarithmic color scale.

debris disks in binaries (see Section 6.2.1), although the invariable plane about which the orbit precesses could also be affected by the gravity of massive planets in the system.

For the model parameters, we further assume a belt opening angle of $5°$, a size-independent catastrophic disruption threshold of 10^7 erg g^{-1} (representing the grains' collisional strength), as well as a grain composition of 1/3 amorphous silicates and 2/3 organic refractories by volume, which determines their Mie-theory-derived optical properties. Four models of different belt dust masses, ABA 1–4, are considered, for which derived quantities are summarized in Table 3. The resulting surface brightness profiles of the different models are compared in Figure 7. Here, the ABA-1 model differs from the other models in having a sharper decline of surface brightness at the inner belt edge. This is because, at that mass, even small dust is effectively ground down to blowout sizes before it can migrate inward past the belt. As a result, further increases in belt mass only enhance the local brightness within the belt, while the interior regions reach saturation (Wyatt 2005).

To give an indication of the plausibility of the ABA models, we also conduct a simplified analysis of total belt mass and collisional lifetimes within the belt, assuming a canonical collisional cascade with a size distribution following a power-law slope of -3.5 (Dohnanyi 1969) extending up to a maximum planetesimal size of 1000 km. Comparing the collisional lifetime of the largest planetesimal to the system age of α Cen (~ 5 Gyr) shows that the ABA-1 model is likely not viable, since even with planetesimals as large as 1000 km, collisions would have inevitably eroded the planetesimal belt to below the ABA-1 level over the system age. In contrast, ABA-2 is marginally consistent with the an-

ticipated level of erosion, while ABA-3 and ABA-4 are more readily compatible with the system's age, only requiring planetesimal masses of a few times that of the Solar System's main asteroid belt. Nevertheless, we retain the ABA-1 model in this analysis for comparison purposes.

For reference, we also include an exozodi model that is similar to the Solar System zodi, even though its radial extent is non-physical around α Cen A. This fiducial "1-zodi" model is derived from the Kelsall et al. (1998) geometrical model for the Solar System's dust cloud, which was fitted to infrared zodiacal light observations by COBE/DIRBE. Here we use the radial surface density distribution approximation derived by Kennedy et al. (2015) for the Kelsall et al. (1998) model. Using the emissivities fitted by Kelsall et al. (1998), we calculate the disk's corresponding surface brightness distribution at 15.5 μm, which is also shown in Figure 7. We then use the same image synthesis pipeline as with our ABA exozodi models, the result of which closely matches the outcome of applying the `zodipic` model—an IDL implementation of the Kelsall et al. (1998) model (Kuchner 2012)—around α Cen A (see Beichman et al. 2020), and likewise inject this 1-zodi model into the MIRI datacubes.

While our ABA exozodi models are not strictly comparable to the Solar System's zodiacal cloud in terms of geometry, it is still useful to define a "zodi level" that quantifies the dust content of the disks relative to the Solar System. Two wavelength-independent metrics for this are the total disk luminosity and the surface density within the habitable zone (HZ). The luminosity-based zodi level is defined as the ratio of the exozodi's fractional luminosity to that of the Solar System's zodiacal

Table 3. Exozodiacal Disk Models

Model	$M_{\rm dust}$ $(10^{-8} M_\oplus)$	$M_{\rm belt}$ $(M_{\rm MAB})$	$T_{\rm coll,1000km}$ (Gyr)	$F_{\rm d,15}$ (mJy)	$F_{\rm d,15}/F_{\star,15}$ $\times10^{-4}$	$\frac{F_{\rm d,24}}{\sigma_{24}}$	$\frac{F_{\rm d,70}}{\sigma_{70}}$	$\frac{F_{\rm d,100}}{\sigma_{100}}$	$L_{\rm d}/L_\star$ $\times10^{-7}$	Z_L	Z_Σ	S/N
ABA 1	20	28	0.88	596	69	1.04	0.29	0.76	94	58	84	78.7
ABA 2	4	5.6	4.40	156	18	0.27	0.07	0.17	27	17	29	52.6
ABA 3	2	2.8	8.80	53	6.1	0.09	0.04	0.09	8.3	5.1	8.4	21.3
ABA 4	1.2	1.7	14.5	20	2.3	0.03	0.02	0.06	3.0	1.8	3.0	5.8
1-zodi	$\cdots$	$\cdots$	$\cdots$	8.8	1.0	0.02	0.02	0.06	1.5	.94	1.0	-0.7

Note—Exozodi models used for injection and derived quantities. Columns: $M_{\rm dust}$, ABA model dust mass parameter (belt mass up to 1 cm grain size); $M_{\rm belt}$, ABA model belt mass up to largest planetesimal (1000 km) in units of Solar System main asteroid belts ($M_{\rm MAB} = 4 \times 10^{-4} M_\oplus$); $T_{\rm coll,1000km}$, collisional lifetime of largest planetesimal; $F_{\rm d,15}$, total disk flux at 15.5 μm; $F_{\rm d,15}/F_{\star,15}$, fractional disk flux at 15.5 μm; $\frac{F_{\rm d,24}}{\sigma_{24}}$, photometric significance (phot. sig.) for MIPS24; $\frac{F_{\rm d,70}}{\sigma_{70}}$, phot. sig. for PACS70; $\frac{F_{\rm d,100}}{\sigma_{100}}$, phot. sig. for PACS100 (all uncertainties from Wiegert et al. 2014); $L_{\rm d}/L_\star$, fractional disk luminosity; Z_L, zodi level by fractional luminosity; Z_Σ, zodi level by Earth Equivalent Insolation Distance (EEID) surface density; and S/N ratios of injection recovery tests with the April 2025 dataset for the case of binary-coplanar disks.
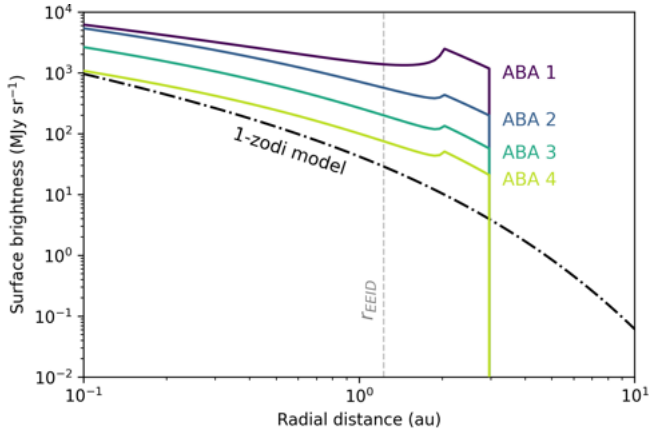
Figure 7. Surface brightness distribution of injected zodi models. ABA-scenario zodis for different belt masses are represented by solid lines. Our fiducial 1-zodi model based on the Kelsall et al. (1998) model is represented by the dash-dot line.

cloud:

$$Z_L = \frac{L_{\rm d}}{L_\star} \Big/ \frac{L_{\rm d,SS}}{L_\odot} \ , \tag{1}$$

while the surface-density-based zodi level is given by the ratio of the disk surface density at the Earth-equivalent insolation distance (EEID), $r_0 = \sqrt{L_\star/L_\odot}$ au—approximately 1.23 au for α Cen A—to that of the Solar System at 1 au ($\Sigma_{0,\rm SS}$):

$$Z_\Sigma = \frac{\Sigma_0}{\Sigma_{0,\rm SS}} \ , \tag{2}$$

with $\Sigma_{0,\rm SS} = 7.12 \times 10^{-8}$ (Kennedy et al. 2015). As discussed by Kennedy et al. (2015), Z_Σ serves as a proxy for

the exozodi's surface brightness in the HZ and is therefore useful for assessing its impact on direct imaging of Earth-like planets. Both definitions of the zodi level are provided in Table 3 for our set of models.

3.4.2. Comparison with Previous Exozodi Searches

The results of the injection-recovery analysis of our various exozodi models, presented in Paper II (Sanghi & Beichman et al. 2025), are summarized by the corresponding S/N values in Table 3. We find that the three brightest injected exozodi models (ABA 1–3) are reliably recovered by our method at S/N $\gtrsim$ 20. The measured S/N for the faintest model, ABA-4, is $\sim$6. However, this S/N level does not constitute a reliable detection as it is consistent with the range of S/N measured in the original image, when no disk model is injected (see Paper II; Sanghi & Beichman et al. 2025). At the low flux level of ABA-4, the image is dominated by PSF subtraction artifacts from α Cen B or the 4QPM transition boundaries. *In summary, these observations are sensitive to emission from an exozodiacal cloud that is coplanar with the binary orbit at a level of $Z_L \approx 5$ or $Z_\Sigma \approx 8$.* This represents an unprecedented sensitivity compared with previous observations and is facilitated by the system's proximity and the model disks' near-edge-on orientation, which our recovery method is tailored to (see Sanghi & Beichman et al. 2025).

It is first worth acknowledging that previous photometric searches have not detected significant excess dust emission at any wavelength (Wiegert et al. 2014; Yelverton et al. 2019). While Wiegert et al. (2014) suggest a Spitzer/MIPS excess at 24 μm at 2.5σ, even our bright-
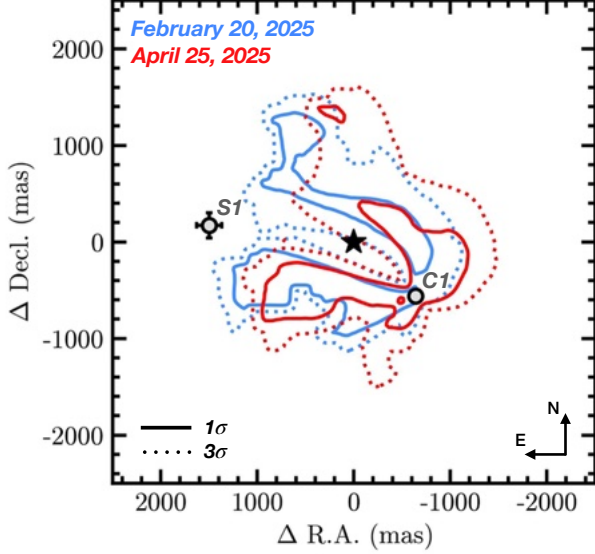
Figure 8. 1σ (solid) and 3σ (dotted) contours showing the sky-projected positions of the $S1+C1$ candidate consistent with a non-detection in the February (blue) and April (red) 2025 observation epochs.

est model disk, ABA-1, yields an excess at 24 μm of only around 1σ (see Table 3). Since the ABA-1 model would have easily been detected by our observations, we can confidently rule out the presence of a static (inclined) exozodi to have caused the reported feature. Excesses of our model disks in the far-IR for *Herschel* PACS70 and PACS100 observations are of even lower significance, consistent with previous non-detections. This means that any circumstellar disk would have to be even more massive than ABA-1 to have shown up in previous mid- and far-IR photometric observations, indicating that our observations which could detect ABA-3 are at least 10 times more sensitive in terms of the belt's dust mass.

This improvement in sensitivity arises because photometric observations do not provide the most stringent limits on the presence of dust, due to calibration uncertainties that limit detectable excesses to typically more the 10% of the stellar flux (Beichman et al. 2005), but with sensitivity approaching 2% in recent studies with JWST (Farihi et al. 2025). By that metric it is clear that our resolved imaging approach is able to improve on that limit by about two orders of magnitude, since we were able to successfully suppress the stellar emission to recover the signal of the ABA-3 model which has an excess of $\sim 0.06\%$ at 15.5 μm (see Table 3). In principle, lower dust levels than simple photometry can be achieved using nulling interferometry to suppress the stellar emission. The largest and deepest survey of this kind was the HOSTS survey which used the LBT interferometer (LBTI) to search for exozodi emission in the
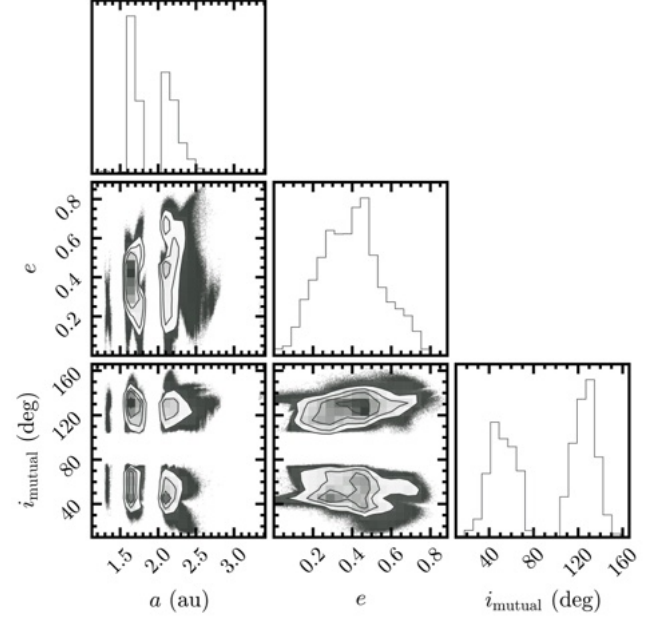
Figure 9. Key parameters for stable planetary orbits fitting the $S1+C1$ astrometry and consistent with the February and April 2025 non-detections. Four orbital families are observed (prograde, retrograde, $a > 2$ au, $a < 2$ au).

habitable zone at 11 μm. While α Cen A wqqqas not included in that survey, due to its Southern hemisphere location and its binarity, the survey results show that the best 1σ sensitivities achieved for (single) solar-type stars reached as low as 0.05% on the null depth, which corresponds to limit of $\sim 0.3\%$ for the total flux required for a detection (Ertel et al. 2018, 2020). That is, our imaging observations achieved a limit at least five times lower than is achievable with nulling interferometry. A similar conclusion is reached by comparing the 5–8 zodi levels of the ABA-3 model (see Table 3) with the best reported zodi limits from the HOSTS survey of $\sim$70 zodis. This is similar to the sensitivity level of previous mid-infrared coronagraphic imaging of α Cen A with VLT/VISIR, since Wagner et al. (2021) reported a resolved source ($C1$) that could be fitted with a $\sim$60 zodi (3σ) exozodi model. Such a disk would be in between our ABA-1 and ABA-2 models, and thus would have been easily detected by our observations. The VLT/VISIR noise level is 5–10 times higher than JWST's. We can thus rule out that $C1$ belongs to a static clump of exozodi material at this level. The comparisons with previous observations demonstrate the dramatic improvement in sensitivity achieved by the JWST measurements.

4. ORBITAL MODELING OF $S1 + C1$

With only a single JWST/MIRI sighting (and non-detections at two other epochs), it is challenging to

Table 4. Key $S1 + C1$ Orbital Parameters

Sightings Used	Orbit Type	a (au)	e	i_{mutual}[a] (°)	i_{sky}[b] (°)	T_{eq}[c] (K)
$S1$, $C1$, & ND[d]	Prograde, $a < 2$ au No RV Constraint	1.66 ± 0.06	0.37 ± 0.12	54 ± 11	55 ± 15 or 124 ± 13	223 ± 5
$S1$, $C1$, & ND	Prograde, $a < 2$ au $K_{RV} < 6$ m/s	1.64 ± 0.07	0.33 ± 0.10	58 ± 11	41 ± 13 or 136 ± 9	223 ± 5
$S1$, $C1$, & ND	Prograde, $a < 2$ au $K_{RV} < 3$ m/s	1.58 ± 0.08	0.27 ± 0.04	70 ± 4	16 ± 5	225 ± 6
$S1$, $C1$, & ND	Prograde, $a > 2$ au No RV Constraint	2.18 ± 0.09	0.43 ± 0.18	49 ± 12	78 ± 26	197 ± 6
$S1$, $C1$, & ND	Prograde, $a > 2$ au $K_{RV} < 6$ m/s	2.14 ± 0.07	0.33 ± 0.14	51 ± 11	68 ± 27	195 ± 5
$S1$, $C1$, & ND	Prograde, $a > 2$ au $K_{RV} < 3$ m/s	2.09 ± 0.02	0.46 ± 0.03	64 ± 6	22 ± 4	200 ± 1
$S1$, $C1$, & ND	Retrograde, $a < 2$ au No RV Constraint	1.68 ± 0.06	0.36 ± 0.12	126 ± 10	64 ± 7 or 132 ± 19	221 ± 6
$S1$, $C1$, & ND	Retrograde, $a < 2$ au $K_{RV} < 6$ m/s	1.67 ± 0.08	0.34 ± 0.10	123 ± 11	49 ± 6 or 144 ± 14	221 ± 6
$S1$, $C1$, & ND	Retrograde, $a < 2$ au $K_{RV} < 3$ m/s	1.65 ± 0.08	0.36 ± 0.07	115 ± 5	162 ± 5	223 ± 6
$S1$, $C1$, & ND	Retrograde, $a > 2$ au No RV Constraint	2.23 ± 0.14	0.43 ± 0.18	126 ± 10	89 ± 24	194 ± 8
$S1$, $C1$, & ND	Retrograde, $a > 2$ au $K_{RV} < 6$ m/s	2.23 ± 0.16	0.32 ± 0.14	122 ± 9	88 ± 29	192 ± 8
$S1$, $C1$, & ND	Retrograde, $a > 2$ au $K_{RV} < 3$ m/s	2.09 ± 0.02	0.64 ± 0.03	115 ± 5	163 ± 5	208 ± 3

[a] Inclination relative to the α Cen AB orbital plane ($i_{\mathrm{AB}} = 79.2430° \pm 0.0089°$, $\Omega_{\mathrm{AB}} = 205.073° \pm 0.025°$ from Akeson et al. 2021).

[b] Inclination relative to the plane of the sky. Bimodal distributions (about $i_{\mathrm{sky}} = 90°$) are presented as two sets of values.

[c] Flux-averaged mean planet temperature for $A_B = 0.3$ (see §5.1)

[d] ND denotes that orbits were checked for consistency with non-detections in the February and April 2025 epochs.

Note—Parameters are reported as mean $\pm$ standard deviation. K_{RV} assumes a planet mass of 100 $M_\oplus$.

uniquely constrain the orbit of $S1$. To make progress, we consider the family of orbits that (a) fit the relative astrometry of $S1$ and the VLT/NEAR 11.25 μm candidate $C1$ (Wagner et al. 2021), which we treat as an earlier detection of the $S1$ object (and in this context, referred to as the $S1 + C1$ candidate); (b) are dynamically stable in the presence of α Cen B; and (c) are consistent with the non-detection of $S1 + C1$ in the February and April 2025 observation epochs. Additionally, we consider the consistency of the candidate's orbits with existing RV upper limits.

4.1. Selection of Stable Orbits

First, we randomly generate 10^7 orbits matching the astrometry of $S1$ and $C1$ (Table 2) using the Orbits For The Impatient (OFTI) algorithm via the `orbitize!` package (Blunt et al. 2017, 2020). We apply the default priors in the `orbitize!` code to the candidate planet's orbital elements and use a Gaussian prior for α Cen A's mass and parallax ($M_{\mathrm{A}} = 1.0788 \pm 0.0029$ $M_\odot$, $\pi = 750.81 \pm 0.38$ mas, from Akeson et al. 2021). Next, we evaluate the stability of the accepted orbits using the N-
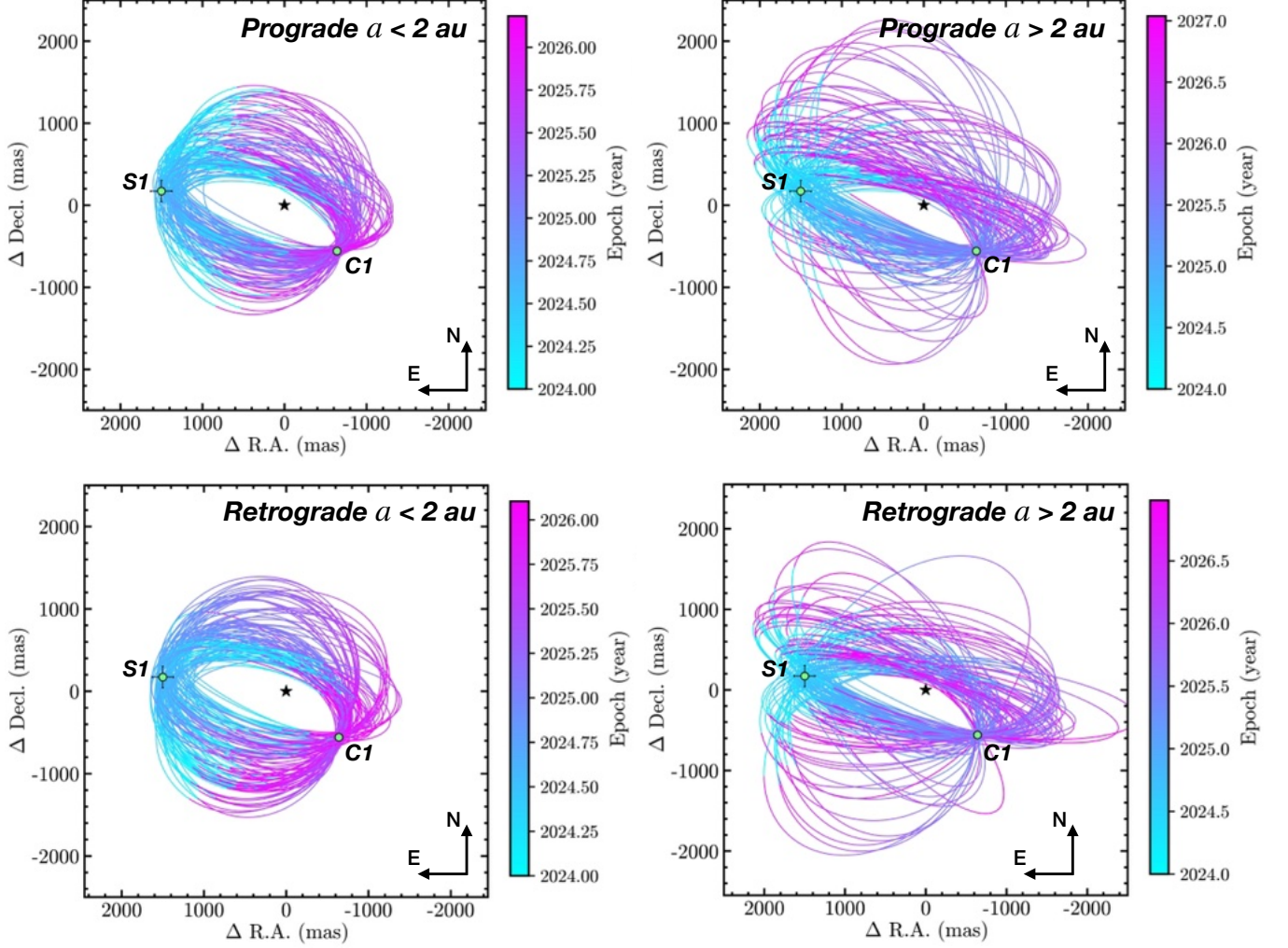
Figure 10. 100 randomly selected stable planetary orbits fitting the $S1+C1$ astrometry (marked as green points) and consistent with the February and April 2025 non-detections, for each orbital family.

body simulation software `Rebound` (Rein and Liu 2012) over million year timescales using the `WHFAST` integrator (Rein et al. 2019). A given simulation is deemed unstable for very high planetary eccentricity ($e_p > 0.95$) or large planetary distances from the host star ($d_p > 5$ au). Previous studies showed that orbits that meet either criterion are very likely to be unstable on billion-year timescales (Quarles & Lissauer 2016, 2018), where more than 90% of orbits stable on a million-year timescale were also stable for billion-year timescales. We find that 30% of the orbits from the initial `orbitize!` sample are dynamically stable.

4.2. Incorporating Constraints From Non-Detections

We investigate which of the above $S1 + C1$ stable orbits are consistent with non-detections in the February and April 2025 observation epochs using the 2D sensitivity maps generated for both epochs in Paper II (Sanghi & Beichman et al. 2025). Specifically, we use

the S/N = 5 sensitivity map (rather than the 5σ significance sensitivity map) to be stricter in eliminating orbits where $S1+C1$ would have been marginally recovered in our follow-up observations. The sensitivity maps provide the minimum point source flux detectable at a S/N = 5 at different sky coordinates around α Cen A. For each of the stable orbits above, we predict the sky position of the candidate planet in the February and April 2025 observations, and check the corresponding location in the sensitivity map to evaluate whether it would have been detected (for a flux of 3.5 mJy). Orbits where the candidate would have been recovered in either of the two epochs are eliminated. *We find that 52% of the stable orbits that fit the $S1 + C1$ astrometry are also consistent with non-detections in both February and April 2025 (Figure 8). There is, thus, an a priori significant chance that, if real, the planet candidate could have been missed in both follow-up observation epochs.*
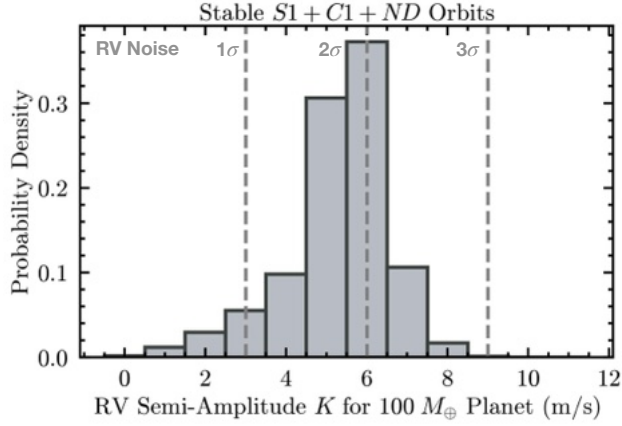
Figure 11. The radial velocity (RV) semi-amplitude of a 100 $M_\oplus$ planet in stable orbits fit to $S1+C1$ and consistent with non-detections in the February and April 2025 epochs. Note that K_{RV} scales linearly with planet mass. The systematic RV noise floor of 3 m/s (1σ; Zhao et al. 2018, Kervella et al., in prep) is shown.

The posteriors for the three key orbital elements (semi-major axis a, eccentricity e, and mutual inclination $i_{\rm mutual}$ with respect to the α Cen AB binary orbit[5]) of the stable orbits consistent with the non-detections (Figure 9) show that there are four families of orbits[6]. They correspond to the number of orbital periods that have elapsed between the VLT/NEAR observations in June 2019 and the JWST detection in August 2024 (either $\sim$1.5 or $\sim$2.5 periods, for $a \approx 1.6$ au and $a \approx 2.1$ au, respectively) and orbits in either the prograde ($i_{\rm mutual} \approx 50°$) or retrograde ($i_{\rm mutual} \approx 130°$) direction (Figure 10). In addition to being significantly inclined, the $S1+C1$ planet candidate is in a moderately eccentric (≈ 0.4) orbit. A summary of the mean orbital parameters for each family (no RV constraint case) is provided in Table 4. Note that all orbits presented are dynamically stable as evaluated previously (§4.1).

4.3. Consistency with RV Limits

To the family of stable orbits consistent with non-detections, we can add a constraint of $K_{RV} < 3$ m s^{-1} (1σ; Butler et al. 2004; Zhao et al. 2018) on the radial velocity of α Cen A, which is also observed in the HARPS RV residuals (Kervella et al., in preparation). This systematic noise floor constrains the minimum mass ($M_p \sin i$) of any planet around α Cen A to

be $< 100\ M_\oplus$ (2σ) or $< 150\ M_\oplus$ (3σ) within ≈ 2 au. Among the dynamically stable $S1 + C1$ orbits consistent with the non-detections, assuming $M_p = 100\ M_\oplus$, we find that 4% of these orbits result in $K_{RV} \leq 3$ m/s, 50% result in $K_{RV} \leq 6$ m/s, and 99.8% of all orbits result in $K_{RV} \leq 9$ m/s (Figure 11, the maximum K_{RV} is ≈ 11 m/s). Table 4 presents orbital parameters for each case. The semi-major axis and eccentricity remain largely unchanged after applying the RV constraints; however, the mutual and sky inclinations vary as the RV constraint becomes stricter (smaller reflex motion). In summary, the astrometric positions of $S1 + C1$ can be fit by dynamically stable orbits consistent with both the non-detections in follow-up observations and existing RV limits. All dynamically stable $S1 + C1$ orbits consistent with non-detections can be retrieved from 10.5281/zenodo.16280658.

5. PHOTOMETRIC MODELING OF $S1 + C1$

In this section, we consider the available photometric data points for the α Cen A planet candidate (JWST/MIRI 15.5 μm and possibly, VLT/NEAR 11.25 μm) to investigate its bulk physical properties. While the photometric data are sparse at the moment, there are some physical constraints that can be applied to aid modeling efforts. First, the effective temperature of the planet candidate is expected to be set by heating from α Cen A. Second, the radius of a mature ($\sim$5 Gyr) gas giant planet cannot significantly exceed 1–1.2 $R_{\rm Jup}$ (allowing for some variations if the planet is rapidly rotating and viewed pole-on, for example) unless it is located in a very tight "Hot Jupiter" orbit, which is not the case as seen in the previous section on orbital modeling. Finally, the mass of the planet must be consistent with the limits set by the radial velocity measurements (Zhao et al. 2018). Subject to these constraints, we examine a range of plausible atmospheric models as well as thermal emission from a Saturn-like particle ring to explain the photometric data.

5.1. Equilibrium Temperature

We use the orbital information to infer the range of plausible effective temperatures for the planet candidate, heated by α Cen A. The equilibrium temperature for a planet on an eccentric orbit depends on the instantaneous stellar input, the planet's thermal inertia, and radiative timescale. For a gas giant planet, any variations of temperature through the orbit are damped by the thermal inertia of the dense H/He atmosphere (Quirrenbach 2022). In such a scenario, the correction to the equilibrium temperature to account for changes in the insolation averaged over an eccentric orbit are small,

---

[5] The mutual inclination is calculated using Equation 19 in Xuan & Wyatt (2020) and using the orbital parameters for α Cen AB in Akeson et al. (2021).

[6] We do not consider the small fraction ($\sim$0.2% of the total number) of $a < 1.5$ au orbits in Figure 9 as they do not agree with $S1$'s relative astrometry within 1σ uncertainties.
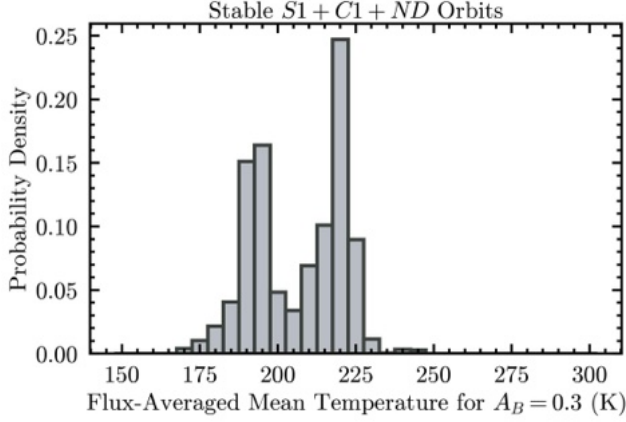
Figure 12. Range of flux-averaged mean planet temperatures for $A_B = 0.3$ corresponding to the orbits described in the preceding section. The lower temperatures in the bimodal distribution correspond to the $a > 2$ au orbits.

only a few percent, for eccentricities up to 0.5 (Johnson & McClure 1976; Quirrenbach 2022). The flux-averaged temperature of a body heated by and orbiting α Cen A in an eccentric orbit, T_{eq}, at a distance d is given by

$$T_{eq} = T_\star \cdot \left(\frac{1 - A_B}{4f} \right)^{1/4} \cdot \sqrt{\frac{R_\star}{d}} \cdot (1 - e^2)^{-1/8}, \quad (3)$$

where $T_\star = 5766$ K (Zhao et al. 2018), $R_\star = 1.2175\ R_\odot$ (Akeson et al. 2021), A_B is the Bond albedo, and full heat re-distribution ($f = 1$) is assumed. Adopting $A_B = 0.3$ (intermediate between the values for most Hot Jupiters and those of the Solar System gas giants), we compute T_{eq} for all $S1 + C1$ stable orbits consistent with the non-detections (§4) and find a bimodal distribution with peaks at ≈ 195 K and ≈ 220 K (Figure 12). The lower temperatures correspond to orbits in the $a > 2$ au families and the higher temperatures correspond to orbits in the $a < 2$ au families (Table 4).

The contributions of additional sources of heat for the planet candidate's temperature are negligible compared to stellar insolation. (1) Residual heat of formation: α Cen A is ~ 5 Gyr old. For a similar internal radiation flux (F) as Jupiter or Saturn, $T_{int} < 110$ K (Li et al 2018), the increase in temperature is negligible, due to $T \propto F^{1/4}$ and the planet candidate's higher expected T_{eq}. (2) Radiation from α Cen B: α Cen B is less luminous than α Cen A by a factor of ~ 3 (Akeson et al. 2021) and at the time of JWST observations was ~ 20 au away from α Cen A. Thus, its contribution to heating is negligible. (3) Tidal heating: the $S1 + C1$ candidate is in an eccentric orbit. However, $\dot{E}_{tide} \propto a^{-15/2}$ (Peale & Cassen 1978) is negligible for $a \sim 2$ au. (4) Heating from radioactivity: this is negligible for Neptune, which

is both much colder than $S1 + C1$ and likely has a larger fraction of radioactive isotopes.

5.2. *Planet Atmospheric Models*

The goal in this section is to obtain first estimates of the planet candidate's fundamental parameters (T_{eff}, radius, and mass) using atmospheric model grids available in literature for cold planets and brown dwarfs. Given the numerous atmospheric parameter degeneracies involved in fitting two photometric data points, particularly in the observationally unexplored low-mass ($\lesssim 200\ M_\oplus$), low temperature (< 300 K) planetary regime (see for example, Crotts et al. 2025), we aim only to provide example scenarios that can explain the observed flux measurements. Detailed atmospheric modeling is appropriate for future studies when additional photometry and/or spectroscopy is available (see §6.3).

We jointly fit the F1550C JWST/MIRI flux and the 11.25 μm VLT/NEAR flux (Table 2), assuming they are related (as indicated by the orbit fits in the previous section). The fitting procedure synthesizes model photometry in the F1550C bandpass (≈ 15.15–$15.85\ \mu$m, using the transmission curve from the SVO filter profile service[7]) and the VLT/NEAR bandpass (≈ 10–$12.5\ \mu$m, constant transmission assumed), and finds the minimum radius ($< 1.2\ R_{Jup}$) that yields a model flux consistent with the measured photometry within 1σ. The effective temperature of the planet is set to 225 K for the atmospheric models fit below, matching that expected for $a < 2$ au orbits (Table 4)[8]. We also restrict the surface gravity (log g, in CGS units) of the models to 2.5–3.0 dex, chosen to yield a planet mass $\lesssim 150$–$200\ M_{Earth}$ to be consistent with radial velocity limits ($M_p \sin i < 150\ M_\oplus$, 3σ; inclined orbits can raise the limit on the true planet mass).

ATMO2020++ (Leggett et al. 2021; Meisner et al. 2023): Using the ATMO2020 models with strong vertical mixing as a starting point, ATMO2020++ modifies the adiabatic ideal gas index γ (and thus atmospheric temperature gradient) to account for the effect of processes responsible for producing a non-adiabatic cooling curve in giant planet and brown dwarf atmospheres. These processes include complex atmospheric dynamics (e.g., zones, spots, waves) due to rapid rotation, compositional changes due to condensation, upper atmosphere heating by cloud decks or breaking gravity waves, etc. Recent modeling with JWST data has shown that this grid provides an improved fit to Y

---

[7] http://svo2.cab.inta-csic.es/theory/fps/
[8] We were unable to fit the photometry with 200 K models for planet radii $< 1.2\ R_{Jup}$.
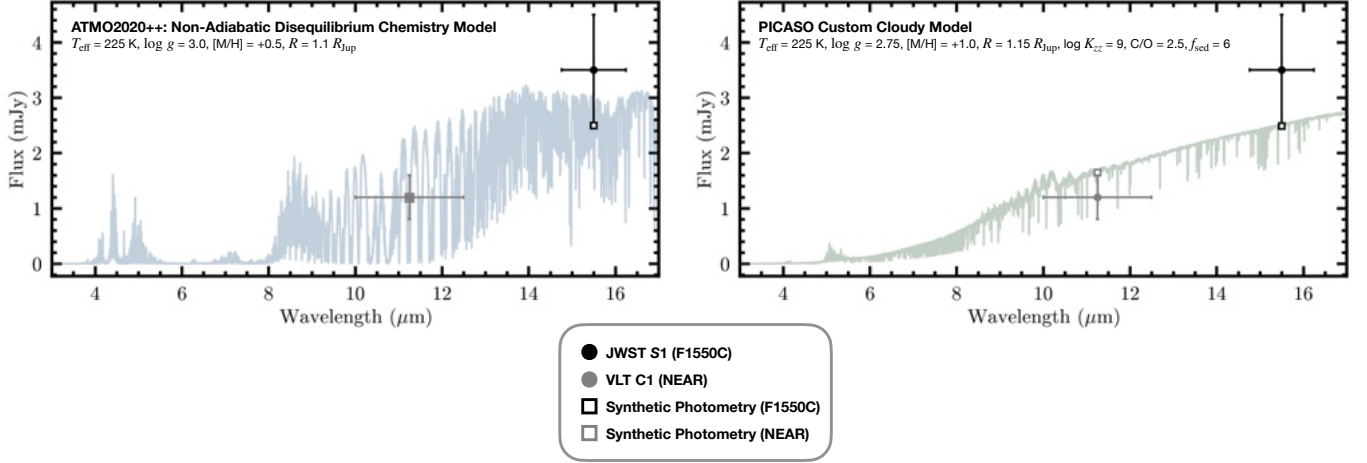
Figure 13. $T_{\rm eff} = 225$ K atmospheric models consistent with the $S1 + C1$ photometry (within 1σ) for a radius $< 1.2\ R_{\rm Jup}$.

dwarf spectra compared to the standard-adiabat models (Leggett & Tremblin 2023, 2024; Luhman et al. 2024). The default ATMO2020++ grid only extends to $T_{\rm eff} = 250$ K, so we generated custom models for $T_{\rm eff} = 225$ K, $\log g = 3.0$ dex, and [M/H] $= +0.5$, $+1.0$. We find that the $T_{\rm eff} = 225$ K, $\log g = 3.0$ dex, and [M/H] $= +0.5$ model agrees with the photometry for a radius of $1.1\ R_{\rm Jup}$ (Figure 13). For the above parameters, the planet candidate would have a mass $\approx 150\ M_\oplus$.

Sonora and PICASO models: The Sonora Flame Skimmer models (Mang et al., in prep) extend the cloud-free Sonora Elf Owl grid (Mukherjee et al. 2024; Wogan et al. 2025) to colder effective temperatures, lower surface gravities, and a broader range of metallicities. These models incorporate rainout chemistry for H_2O, CH_4, and NH_3—even in cloud-free atmospheres—similar to the treatment in Sonora Bobcat. They also address the underestimation of CO_2 found in the Sonora Elf Owl models (Mukherjee et al. 2024), which has since been revised in Wogan et al. (2025). In addition, we generated a custom grid of cloudy models using PICASO (Batalha et al. 2019; Mukherjee et al. 2023). This grid spans effective temperatures of $T_{\rm eff} = 200$ and 225 K, surface gravities of $\log g = 2.75$ and 3.0 dex (cgs), eddy diffusion coefficients $K_{zz} = 10^2$ and 10^9 cm^2 s^{-1}, metallicities of [M/H] $= +0.5$ and $+1.0$, and a C/O ratio of 2.5 (relative to solar). Cloudy models have $f_{\rm sed} = [4, 6, 8]$, with H_2O as the only condensing species. We find that the $T_{\rm eff} = 225$ K, $\log g = 2.75$ dex, [M/H] $= +1.0$, $\log K_{zz} = 9$, C/O $= 2.5$, $f_{\rm sed} = 6$ model agrees with the photometry for a radius of $1.15\ R_{\rm Jup}$ (Figure 13). For the above parameters, the planet would have a mass $\approx 90\ M_\oplus$.

Additional models applicable to cool giant planets: We also experimented with fitting the photometry using the Sonora Bobcat cloudless, chemical equilibrium model grid (Marley et al. 2021), the ATMO2020 solar metallicity, disequilibrium chemistry model grid (Phillips et al. 2020), the patchy water cloud models of Morley et al. (2014), and a new grid of self-consistent models by Lacy & Burrows (2023) that incorporate both the effects of water clouds and disequilibrium chemistry. However, we did not find suitable solutions with these grids, as they all required a $T_{\rm eff} \geq 250$ K to fit the photometry for a radius $< 1.2\ R_{\rm Jup}$.

5.3. Planet Ring System Models

The previous section presented example planet models which can reproduce the brightness of $S1 + C1$, but required planet radii $\approx 1.1\ R_{\rm Jup}$ (driven by the observed F1550C brightness), more commonly observed for hotter planets, but plausible if a rapidly rotating planet is viewed closer to pole-on (the observed surface area can be higher). Alternate explanations for the F1550C brightness include (1) a knot of exozodiacal emission; or (2) a smaller planet with a circumplanetary ring. Given the lack of exozodi detection reported in §3.4, we do not consider the exozodi knot interpretation further, except to note that this would require the knot to dominate the exozodi emission, and for the knot to orbit the star with similar constraints to those reported for the planet scenario (§4) and to have only been detected at one epoch of our observations.

For an interpretation of the emission as circumplanetary material, a straight-forward model is to consider an optically thick ring. A ring is not expected to have significant thermal inertia (as opposed to a gas giant planet, as discussed in §5.1). Thus, the ring temperature at the $S1$ and $C1$ detection epochs will be the instantaneous equilibrium temperature calculated for the true planet-star separation at those epochs. For each stable $S1 + C1$ orbit consistent with the non-detections in the
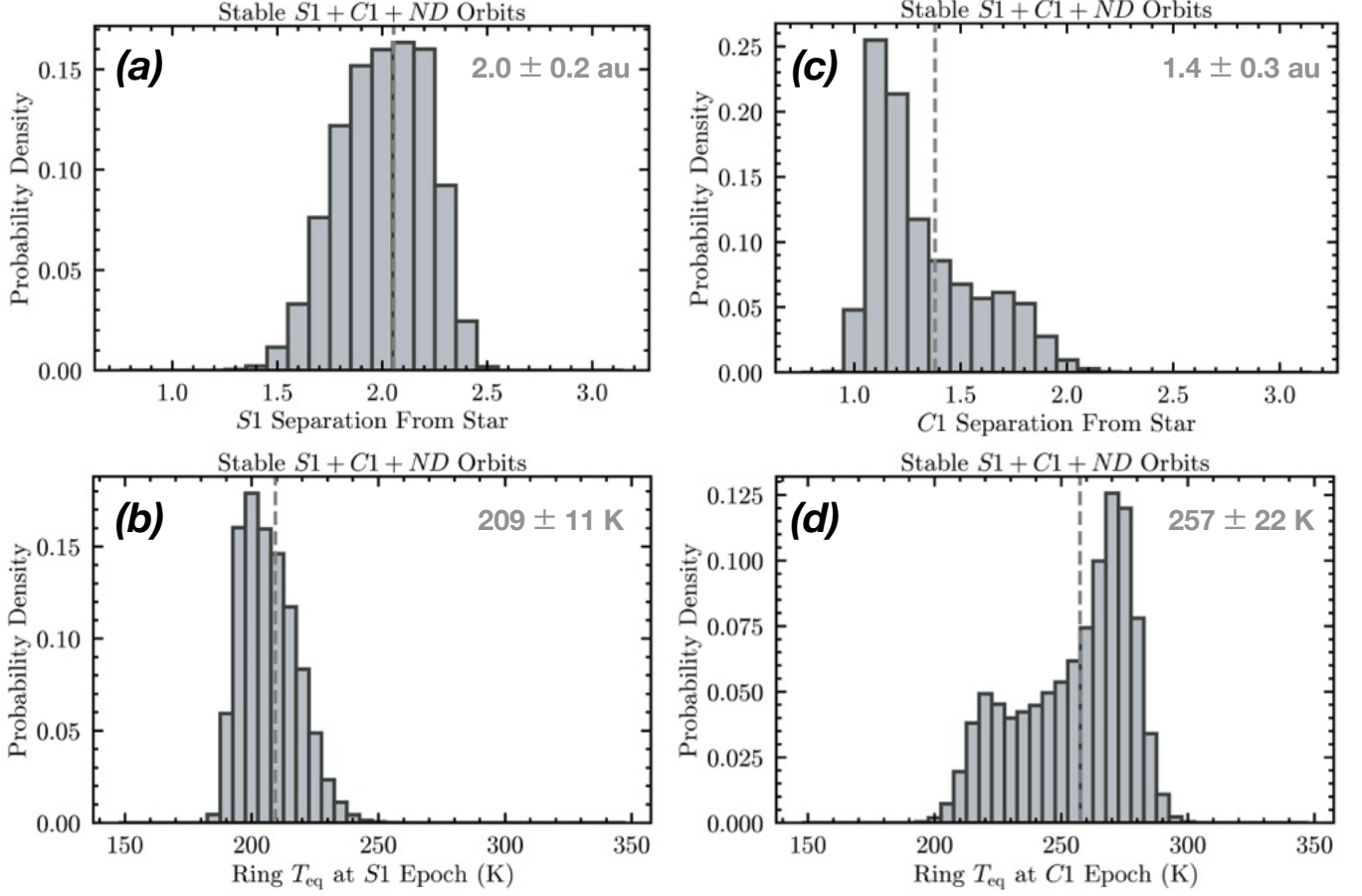
Figure 14. Range of (true) star-planet separations (top) and instantaneous temperatures (bottom) for a planetary ring with $A_B = 0.1$, no thermal inertia, and $f = 1$, seen at the epochs of $S1$ (left) and $C1$ (right) based on the stable orbits consistent with non-detections in the prograde $a < 2$ au family as described in §4. The mean value of each distribution is marked with a dashed line and noted with the standard deviation in the top right corner of each panel.

prograde $a < 2$ au family, we calculate the planet-star separation and the corresponding equilibrium temperature, assuming $A_B = 0.1$ (similar to asteroids) and $f = 1$ (Figure 14). Orbits with $a < 2$ au are favored as they yield a higher planet $T_{\rm eq}$, which is required to better fit the F1550C brightness (the prograde and retrograde scenarios yield similar separation distributions and mean values). We find that an optically thick circumplanetary ring would be hotter at the $C1$ epoch ($T_{\rm eq} = 257 \pm 22$ K) than at the $S1$ epoch ($T_{\rm eq} = 209 \pm 11$ K).

We modeled the observed $S1 + C1$ photometry using various 225 K planet atmospheric models (grids discussed in §5.2) combined with a constant surface area (free parameter) blackbody ring with a temperature of 257 K for the VLT/NEAR 10–12.5 μm flux and a temperature of 209 K for the F1550C flux. The photometry agrees, within 1σ uncertainties, with a Sonora Flame Skimmer clear, equilibrium, $T_{\rm eff} = 225$ K, $\log g = 3.0$ dex, [M/H] $= +1.0$, and C/O $= 1.5$ model for a planet radius of 1 $R_{\rm Jup}$ (corresponding to ≈ 120 $M_{\oplus}$), together

with a ring that has a cross-sectional area equivalent to a face-on disk of radius $\approx 64{,}000$ km or ≈ 0.9 $R_{\rm Jup}$ (Figure 15). This is $\sim$ half the cross-sectional area of Saturn's rings, which extend to 140,000 km (plus a more tenuous, more distant distribution). Planetary rings lie in their planet's Roche zone from 1.4–2.5 R_p, so this explanation seems plausible. If the planet candidate is closer to the star at the $S1$ epoch or farther at the $C1$ epoch than the mean separation presently assumed at each epoch, then the agreement with the measured photometry improves.

We stress that the ring model discussed above is highly simplified. Geometrical effects make it challenging to develop a fully comprehensive and accurate optically thick ring model. The inclination of the ring with respect to the star affects the ring's temperature. The inclination of the ring to our line-of-sight together with shadowing of the ring by the planet affects the inferred size and visible emitting area. Additionally, a ring could both shade the planet from starlight, reducing planet temperature,
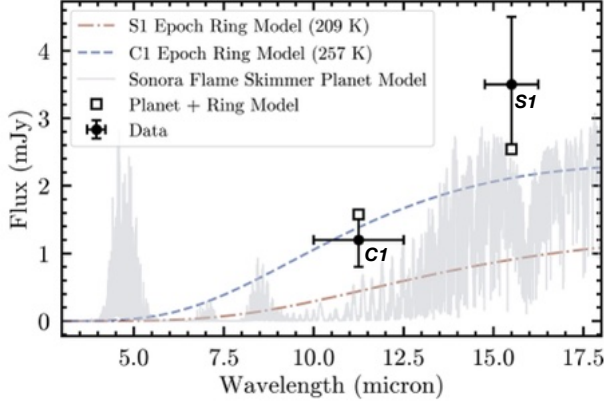
Figure 15. Blackbody (BB) emission from a circumplanetary ring for a total cross-sectional area equivalent to the half the face-on cross-sectional area of Saturn's rings together with a fiducial planet atmospheric model ($T_{\rm eff}$ = 225 K, log g = 3.0 dex, [M/H] = +1.0, C/O = 1.5, R_p = 1 $R_{\rm Jup}$). Each component contributing to the total model VLT/NEAR and F1550C flux (squares) is shown. There are two BB components as the ring temperature is different for each detection epoch, depending on the planet-star separation in Figure 14.

and block planet light towards the observer. In the absence of strong constraints on the planet candidate's orbit and with only two photometric points, the problem is highly unconstrained. Overall, the key takeaway of the analysis presented above is that a circumplanetary ring around the $S1 + C1$ planet candidate is a plausible hypothesis to explain the higher F1550C brightness for a smaller planet than inferred just using atmospheric models. A summary of the inferred mass and radius of the $S1 + C1$ candidate from both atmospheric and ring models, as compared with the cold transiting planet population, is presented in Figure 16.

For completeness, we consider an alternative model for circumplanetary material, where the cross-sectional area derived above comes from an optically thin dust distribution, such as one that might arise from the grinding down of a cloud of irregular satellites orbiting the planet (Kennedy et al. 2011). Such a cloud could extend out to roughly half the Hill radius of the planet ($R_{\rm H} \sim 0.09$ au radius for a low eccentricity, 100 $M_\oplus$ planet at 2 au), which would correspond to a distribution with optical depth $\sim 5 \times 10^{-5}$. Small grains with realistic optical properties, in models in which the dust is optically thin, are heated above blackbody temperature. This increases the flux in the VLT/NEAR bandpass and makes it more challenging to simultaneously fit the $S1$ and $C1$ photometry, specifically because the ring is expected to have a higher temperature at the $C1$ detection epoch than the $S1$ detection epoch from planet-star separation calcula-
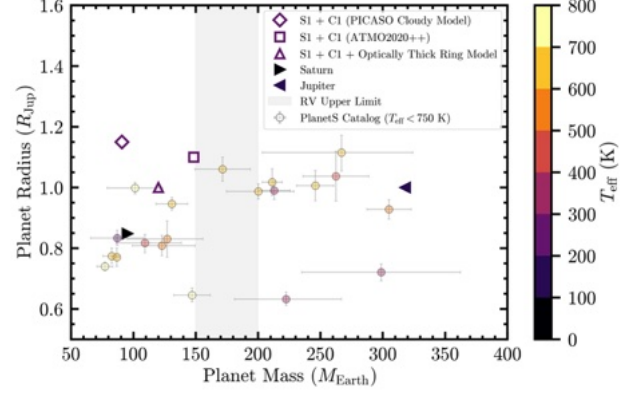
Figure 16. Observed masses and radii derived from transit observations for planets cooler than 750 K (from the PlanetS Catalog, Müller et al. 2024) are shown along with the properties of the $S1 + C1$ planet candidate inferred from the different models. The shaded area shows the approximate range of RV upper limits, depending on the exact inclination of the candidate's orbit. The positions of Saturn and Jupiter are included.

tions (Figure 14). This would require the dust distribution to be truncated to avoid the presence of μm-sized dust. This is in addition to the challenge of retaining the irregular satellites given their expected collisional erosion.

6. DISCUSSION

We start by investigating possible mechanisms to explain the high eccentricity and inclination orbits inferred for the $S1 + C1$ candidate in a close binary system like α Cen AB. We then briefly discuss the prospects for other planets or an exozodiacal disk around α Cen A in the presence of the $S1 + C1$ candidate, and end with a discussion of implications of a gas giant in α Cen AB system in relation to theories of planet formation in binary systems.

6.1. Planetary Companions

6.1.1. Secular Dynamics of S1 + C1 Planet Candidate

Table 4 reveals that the best fitting orbits for $S1 + C1$ consistent with the non-detections are significantly inclined with respect to the α Cen AB binary orbital plane and eccentric, which naturally leads one to suspect that the planet candidate might undergo von Zeipel-Kozai-Lidov (vZKL) oscillations. The von Zeipel-Kozai-Lidov mechanism is a secular gravitational effect in hierarchical triple systems whereby a distant companion's torque drives a periodic exchange between the inner orbit's eccentricity and inclination. This dynamical exchange can help explain why the candidate planet's best-fitting orbits exhibit moderate eccentricity, as it cycles through a wide range of eccentricities and mutual inclinations
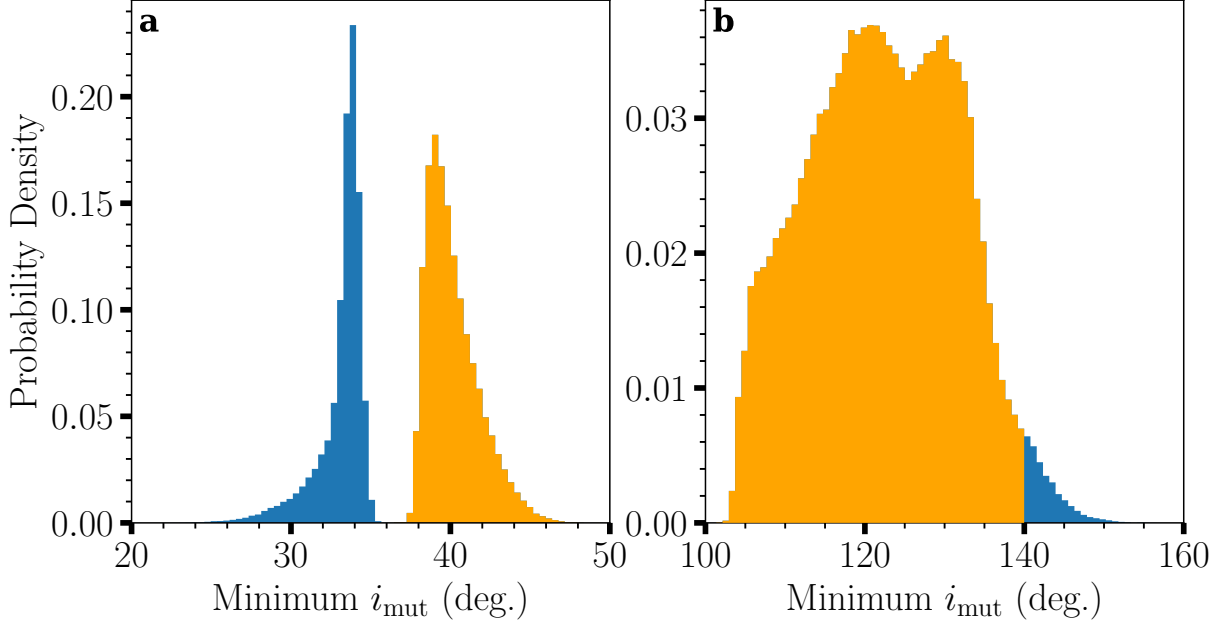
Figure 17. Range of minimum mutual inclination i_{mut} experienced by the prograde (a) and retrograde (b) planet in the inner orbit ($a < 2$ au family). Orbits colored yellow represent the i_{mut} range within the von Zeipel-Kozai-Lidov (vZKL) regime that would produce large amplitude oscillations, while blue denotes i_{mut} values that would have much lower oscillations.

(von Zeipel 1910; Kozai 1962; Lidov 1962; Ito & Ohtsuka 2020). In the test particle approximation (Naoz 2016) for vZKL oscillations, the less massive body ($S1 + C1$) will have a minimum mutual inclination i_{mut} relative to the more massive binary, which is approximately 39.2° for prograde and 141.8° for retrograde orbits. Figure 17 shows the probability density of minimum inclination attained during our N-body stability simulations selecting on the stable orbits that fit $S1 + C1$ and are consistent with non-detections. The minimum mutual inclination shows that a majority of orbits undergo vZKL oscillations, likely to be large amplitude, in the test particle approximation and consistent with the candidate's present configuration.

6.1.2. Prospects For Other Planets Orbiting α Cen A

The Hill Radius, R_H, gives a measure of the relative gravitational influence of two bodies on a third and can be used to identify regions in semi-major axis for the stability of a third body. We use this to assess the possibility that another planet might exist in the Habitable Zone (HZ) of α Cen A given the presence of a planet with the properties of $S1 + C1$. The Hill Radius, R_H is given by:

$$R_{\mathrm{H}} \approx a(1-e) \sqrt[3]{\frac{m_p}{3(m_* + m_p)}}. \qquad (4)$$

Given the best-fit semi-major axis, a, and eccentricity, e, for each of the potential orbital families (Table 4), using the host star mass ($m_* = 1.08$ M$_\odot$), and assuming a candidate planet mass ($m_p \sim 100$ M$_\oplus$), the Hill Radius R_H for semi-major axis, a=1.62–2.16 au and eccentricity ∼0.4, ranges from 0.044–0.060 au. Quarles, Lissauer & Kaib (2018) argue that for stability in a coplanar system, a buffer zone of $\approx 7.5\,R_H$ is required to establish stable orbits in a two planet system. Thus, it is unlikely for there to be any other planets between $a(1-e)-7.5R_{\mathrm{H}}$ and $a(1+e)+7.5R_{\mathrm{H}}$, i.e., from 0.6 au to 3.5 au, depending on the value of a. *Thus, assuming the $S1 + C1$ candidate is real, there are probably no other planets within or exterior to α Cen A's HZ.*

These arguments are bolstered with numerical simulations which show, with the parameters of $S1 + C1$, there are no stable orbits exterior to ∼0.5 au (Figure 18). These simulations use the N-body simulation package `Rebound` with the `IAS15` integrator, where the massive bodies (binary + $S1 + C1$) begin with the mean orbital parameters from the $K_{\mathrm{RV}} < 3$ m/s cases in Table 4 for $S1+C1$ and stellar parameters from Akeson et al. (2021). The putative second planet begins as a test particle on a slightly eccentric orbit ($e_p^* = 0.05$) that is apsidally aligned and coplanar with $S1 + C1$, where we vary the putative second planet semi-major axis a_p^* from $0.25 - 3$ au with steps of 0.001 au and initialize the mean anomaly of the body from $0° - 359°$ in steps of 1°. The simulations are evolved for 1 Myr, where an individual simulation is stopped depending on the state of the test planet, which can either be ejected (distance r_p^* of the test planet exceeding 5 au), have high eccen-
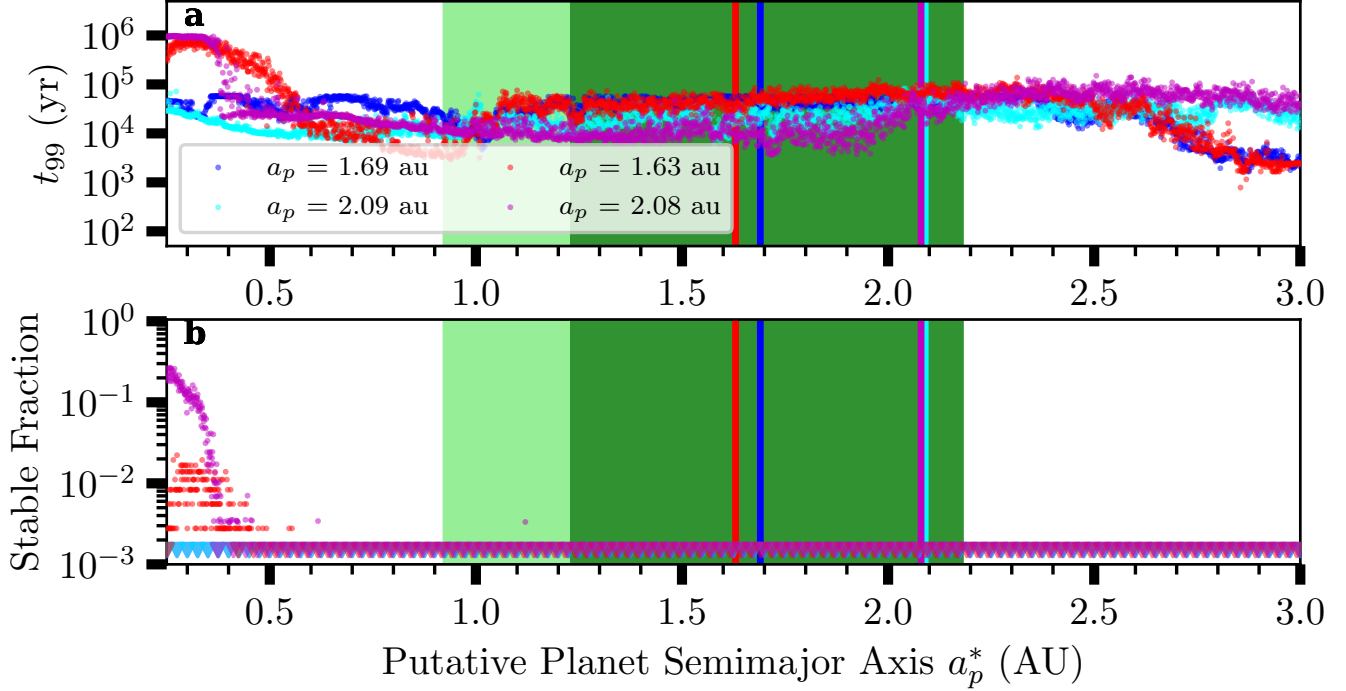
Figure 18. The planet candidate is initialized using the mean values from Table 4 with $K_{\mathrm{RV}} < 3$ m/s, where the color-coded points denote the planet candidate with a prograde (blue/cyan) or retrograde (red/magenta) orbit. The top panel shows the lifetime t_{99} when 99% of the test particles are unstable, while the bottom panel measures the fraction of stable particles for a given initial semi-major axis. The triangles denote upper limits for the stable fraction due to the finite number of trials (360) per semimajor axis. The light green region denotes the optimistic HZ, while the dark green represents the more conservative HZ.

tricity ($e_p^* > 0.95$), or collide with either $S1 + C1$ or the host star.

From these simulations, we calculate the lifetime t_{99} when 99% of the test particles are unstable (in Figure 18a) and the fraction of test particles that are stable for a given semi-major axis (in Figure 18b). For $a_p^* \gtrsim 0.5$ au, virtually all test particles are unstable within 10^5 yr, while for $a_p^* \gtrsim 0.4$ au very few remain in orbit for 1 Myr. The prospects for stability for the test particles increase for $a_p^* \lesssim 0.4$ au, but only when considering a retrograde-orbiting planet candidate. In summary, Figure 18b strongly suggests that the region exterior to ~0.4 au will be inhospitable to any other planets in the presence of $S1 + C1$. The dynamics of the α Cen AB system were already known to be inhospitable to planets outside of ~3 au (Quarles & Lissauer 2018).

6.1.3. *Planets in Binary Systems*

Planets in multiple star systems are not rare. As of this writing, the NASA Exoplanet Archive (Christiansen et al. 2025) lists over 500 such systems, although their number decreases with the number of stars (only 71 in triple systems such as α Cen AB + Proxima Cen,

i.e., α Cen ABC, but stellar companions that are as intrinsically-faint as Proxima Cen may not have been identified yet), including cases like Kepler-132 (KOI-284) where planets have been found in circumstellar orbits about both stars (Lissauer et al. 2014). There is strong observational evidence and robust physical arguments suggesting that for systems with $a < 100$ au, the formation of planets larger than sub-Neptunes in stable configurations is suppressed in multiple systems (Kraus et al. 2016; Moe & Kratter 2021; Dupuy et al. 2022; Sullivan et al. 2024). Moe & Kratter (2021, their Figure 3) describe a suppression factor of 0.4 for a binary system with α Cen AB's semi-major axis of 23 au. Yet although there is observational evidence for the suppression of planet formation in binary systems, there are numerous analyses of multiple star systems which show islands of stability close to either or both of the stars in multiple systems (Quarles & Lissauer 2016, 2018). Two systems in particular, HD 196885 AB + HD 196885 Ab and γ Cep AB + γ Cep Ab, are notable for their similarity in S-type orbital architectures to the candidate α Cen AB + $S1 + C1$ system (Table 5). In each case, the stellar system is a close, eccentric binary and hosts a moderately eccentric planet that is inclined with re-

Table 5. Known S-type Planetary Systems with Similar Orbital Architecture as α Cen AB + S1 + C1

Planetary System	a_{A-B} (au)	e_{A-B}	a_{A-Ab} (au)	e_{A-Ab}	i_{mutual} (°)	References
α Cen AB + S1 + C1 Candidate	≈23	≈0.5	≈1.6 or ≈2.1	≈0.4	≈50 or ≈130	1, 2
HD 196885 AB + HD 196885 Ab	≈21	≈0.4	≈2.6	≈0.5	≈25	3
γ Cep AB + γ Cep Ab	≈19	≈0.4	≈2.1	≈0.1	≈114	4

Note—The orbital parameters are generally well-constrained in all cases but are quoted without uncertainties for the purposes of an approximate, order-of-magnitude comparison.

References—(1) Akeson et al. (2021); (2) This work; (3) Chauvin et al. (2023); (4) Huang & Ji (2022).

spect to the stellar binary orbital plane (prograde or retrograde). Thus, the existence of an exoplanet with the properties of $S1 + C1$ in the α Cen AB system is not impossible.

6.2. *Exozodiacal disks*
6.2.1. *Exozodiacal Disks in Binary Systems*

While the formation of circumstellar sub-Neptunes and larger planets appears to be significantly suppressed in close binaries like α Cen AB, the fate of the smaller bodies that constitute terrestrial planets and debris disks is more nuanced. On the one hand, there has so far been no clear detection of circumstellar debris disks in binaries of separations < 100 au by means of infrared excess (Trilling et al. 2007; Yelverton et al. 2019). But recent observational findings suggest that the presence of circumstellar super-Earths in such binaries is relatively less suppressed than that of sub-Neptunes (Sullivan et al. 2024). This implies that the early stages of planet formation, that is, planetesimal formation and accretion, remain relatively effective.

It is thus reasonable to assume that debris disks can form and exist around these objects, with the caveat that they must lie within the stable region around either stellar component, stretching only a small fraction of their separation, e.g., ∼12% in the case of α Cen AB (Thebault et al. 2021; Cuello & Sucerquia 2024). For binaries with similar separations, this suggests that only asteroid belt analogues within a few AU of each star are dynamically viable as circumstellar debris disks. Any dust produced from them would be relatively warm (∼ 100–300 K), exozodiacal dust, and would emit predominantly in the mid-infrared—where it is outshone by the star—potentially explaining the lack of photometric detections.

Finally, recent observational studies indicate that the orbits of planets orbiting one of the stars in binary (an S-type exoplanet) are roughly aligned with the binary orbit, particularly for separations below ∼ 100 au. Astro-

metric monitoring of *Kepler* planet hosts in binaries has shown that mutual inclinations are typically small, likely within 0–30° (Dupuy et al. 2022; Lester et al. 2023). These findings suggest that long-lived debris disks might exist and might be aligned with binary orbital plane.

6.2.2. *Can an Exozodi Disk and an $S1 + C1$-like Planet Coexist Around α Cen A?*

The prospects of finding a stable debris disk orbiting a star in a binary system must also be considered in the context of the presence of planets. Figure 18 shows effect of a planet on the possibility of stable orbits either for other planets or for particles in a disk. This shows that even if a planetesimal belt was able to form in this system it would not be able to survive in the face of dynamical perturbations from both α Cen B, which prevents orbits surviving beyond ∼ 2.8 au (Quarles & Lissauer 2016), and a planet like the $S1 + C1$ candidate which causes an unstable region that extends to within ∼0.4 au of α Cen A. While a planetesimal belt could survive interior to the planet, the current JWST/MIRI observations are not sensitive to any possible exozodi so close to the star.

6.3. *Future Opportunities with α Cen A*

The most pressing task for further work is to capture a second sighting of $S1$ with JWST. Figure 19 identifies an excellent opportunity in August 2026 to recover $S1$ based on the family of stable $S1 + C1$ orbits consistent with non-detections described in §4. Around this date, the separation exceeds ∼1″ and the predicted location is clear of the 4QPM boundaries. There is an urgency to this given the rapid approach of α Cen A to the known background star denoted KS5 (Kervella et al. 2016). Between mid-2027 and mid-2028, the two will be within 3″ of one another. We note here that if $S1$ is unrelated to $C1$, then the orbits are much less constrained and there is significant uncertainty in its position at any given observation date. Additionally, there
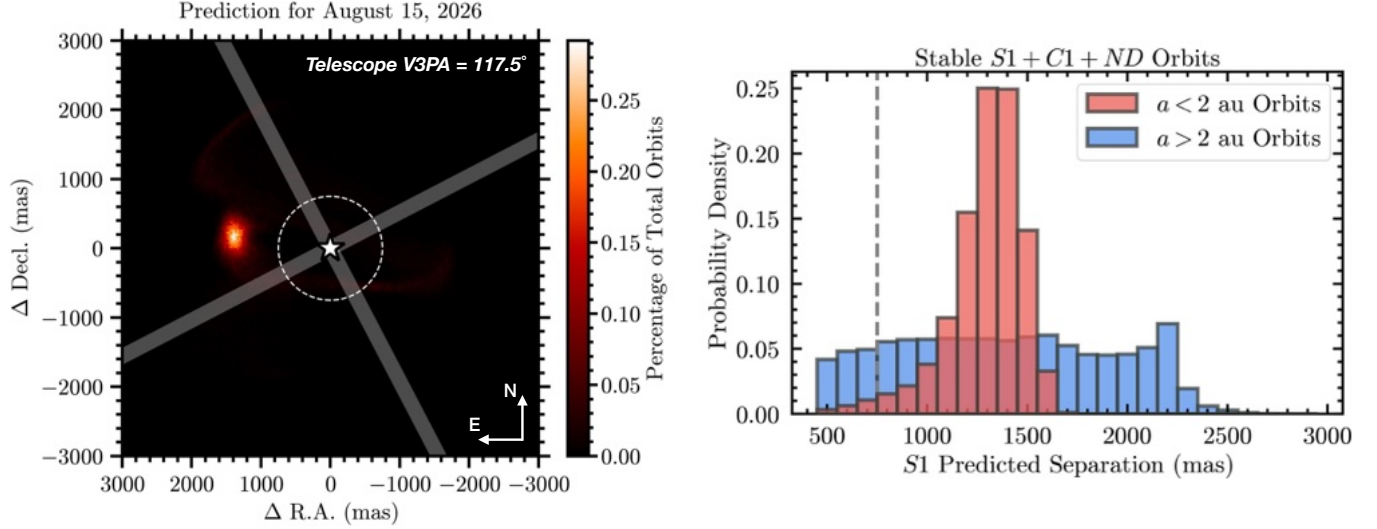
Figure 19. A prediction for the location of $S1$ based on the family of dynamically stable orbits for $S1 + C1$ consistent with the non-detections in 2025 suggests that $S1$ will be well-positioned for recovery in August 2026. *Left:* predicted position in sky coordinates. The approximate orientation of the 4QPM transition boundaries at the selected example observation date is shown as a shaded region. The dashed circle marks $0\farcs75$ separation. *Right:* Histogram of the predicted separation of $S1$ in August 2026 for the two orbital semi-major axis families. A dashed line marks $0\farcs75$ separation. The $a < 2$ au orbits constitute a greater fraction of the total number of orbits and are also favored based on photometric modeling in §5.

are numerous opportunities to follow-up the detection of the candidate exoplanet for further characterization with upcoming and future facilities:

- The clear photospheric model has higher flux between 4–5 μm (Figure 15) compared to the non-adiabatic and cloudy models (Figure 13). NIR-Cam coronagraphy could serve as a powerful diagnostic tool for the different models presented.

- The coronagraphic instrument on the Nancy Roman Space Telescope has a mask specifically designed to work in the presence of a binary star system (Bendek et al. 2021) and could be used to detect reflected visible light from a gas giant around 1–2 au.

- The METIS instrument on the European Extremely Large Telescope (EELT) should be capable of spectroscopic observations of the $S1$ candidate (Birkby & Parker 2024) and could even look for radial velocity shifts in the motion of the planet due to the presence of an exomoon.

- Direct mass measurements should be possible with additional RV monitoring and with differential astrometry at millimeter wavelengths with ALMA (Akeson et al. 2021), or at visible wavelengths with the proposed Toliman (Tuthill et al. 2018) or SHERA (J. Christiansen, private comm.) space telescopes.

- Finally, the proposed Habitable Worlds Observatory (HWO) could, if equipped with appropriate binary star rejection capabilities, search for terrestrial-sized planets which might be found within the α Cen A system despite the pessimistic concerns about the stability of orbits exterior to 0.4 au (§6.1.2).

7. CONCLUSIONS

We conducted JWST/MIRI F1550C coronagraphic imaging observations of the nearest solar-type star, α Centauri A, over three epochs between August 2024 and April 2025 to directly resolve α Cen A's habitable zone and perform a deep search for planets and exozodiacal disk emission. The key results from our program are summarized below.

Detection of a candidate gas giant exoplanet in orbit around our nearest Sun-like star, α Cen A. We detected a point source ($S1$) in the August 2024 epoch of JWST/MIRI 15.5 μm coronagraphic imaging. Detailed analysis, including various tests, presented in Paper II (Sanghi & Beichman et al. 2025) show that the source is unlikely to be a detector or speckle artifact. We definitively show that $S1$ is neither a foreground nor a background object. However, with only a single sighting by JWST, the candidate cannot be unambiguously confirmed as a bona fide planet.

Deep upper limits on an exozodiacal disk around α Cen A. These observations have set stringent upper bounds on the presence of extended "exo-

zodiacal" dust disk in the habitable zone of α Cen A. A limit of < 5–$8\times$ the dust level within our own zodiacal cloud (for a disk coplanar with the α Cen AB orbit) is a factor of $\gtrsim 10$ more sensitive than those set by either photometric or interferometric methods toward more distant stars. Simulations show that for a planet with the candidate's properties, it is unlikely that a debris disk could remain stable and survive the planet's dynamical influence unless located within 0.4 au of the star.

Orbital properties of the α Cen A planet candidate. By linking the sighting of JWST/MIRI $S1$ to another candidate, $C1$, detected by the VLT/NEAR experiment in 2019, we found a set of dynamically stable orbits. 52% of the stable orbits were consistent with a non-detection of the planet candidate in the February and April 2025 epochs, indicating that it was likely missed in both follow-up observations due to orbital motion. The $S1+C1$ candidate is in a highly inclined ($\approx 50°$ or $\approx 130°$ with respect to the α Cen AB binary orbital plane) and eccentric (~ 0.4) orbit, not unlike other S-type planets in close binary systems (e.g., HD 196885 Ab and γ Cep Ab), and is expected to undergo large amplitude von Zeipel-Kozai-Lidov (vZKL) oscillations.

Physical properties of the α Cen A planet candidate. $S1+C1$'s effective temperature is set by heating from α Cen A and is expected to be ~ 225 K based on the candidate's orbital properties. We found plausible atmospheric model solutions to the $S1+C1$ photometry for a planet radius between ≈ 1.1–1.15 $R_{\rm Jup}$ and mass between 90–150 $M_{\oplus}$ (consistent with RV limits). Alternatively, we showed that a simplified optically thick ring with a cross-section equivalent to half of Saturn's ring could increase the mid-infrared flux of a smaller (~ 1 $R_{\rm Jup}$) planet to explain the estimated photometry.

Importance of a confirmed planet around α Cen A. A confirmation of the $S1$ candidate as a gas giant planet orbiting our closest solar-type star, α Cen A, would present an exciting new opportunity for exoplanet research. Such an object would be the nearest (1.33 pc), coldest (~ 225 K), oldest (~ 5 Gyr), shortest period (~ 2–3 years), and lowest mass ($\lesssim 200$ $M_{\oplus}$) planet imaged in orbit around a solar-type star, to date. Its extremely cold temperature would make it more analogous to our own gas giant planets and an important target for atmospheric characterization studies. Its very existence would challenge our understanding of the formation and subsequent dynamical evolution of planets in complex hierarchical systems. Future observations will confirm or reject its existence and then refine its mass and orbital properties, while multi-filter photometric and, eventually, spectroscopic observations will probe its physical nature.

AUTHOR CONTRIBUTIONS

APPENDIX

A. DETAILS OF THE OBSERVATION STRATEGY

A.1. *Reference Star Selection*

For stars as bright as α Cen A ([F1550C] = -1.51 mag), the selection of reference stars is limited. The IRAS Low Resolution Spectrometer (LRS) Catalog (Olnon et al. 1986) was used to identify potential reference stars: $F_\nu(12\ \mu m) > 50$ Jy within $20°$ of α Cen A, clean Rayleigh-Jeans photospheric emission, constant ratio ($<10\%$) of LRS brightness ($F_{\alpha\ \text{Cen A}}/F_{\text{star}}$) across the F1550C band, a low probability of variability during the 300 day IRAS mission (VAR $< 15\%$), and no bright companions within $100''$. These criteria resulted in the selection of ϵ Mus ([F1550C] = -1.3 mag), a long period variable star located $17°$ away on the sky with a K band variability $\lesssim 0.5$ mag (Murakami et al. 2007; Tabur et al. 2009). The ratio of the LRS spectra of the (unresolved) α Cen AB system to these stars is constant across the F1550C bandpass to $< 1\%$ which means that the effects

Table A1. Position of α Cen A at JWST Observation Epochs

Date	JD	R.A. (deg)	R.A.[a] (sec)	Decl. (deg)	Decl.[b] ($''$)
8/10/2024	2460750.363	219.84748601	(23.3967)	−60.83161739	(53.8226)
2/20/2025	2460727.234	219.8472157	(23.3318)	−60.8317325	(54.2370)
4/25/2025	2460790.995	219.8464966	(23.1592)	−60.83177278	(54.3820)
4/25/2025	2460791.2344	219.8464935	(23.1584)	−60.8317725	(54.3813)

Note—[a]Relative to $\alpha = 14^h\ 39^m$. [b]Relative to $\delta = -60°\ 49'$. Positions incorporate proper motion and parallax as seen from vantage point of JWST.

of wavelength mismatches in the reference star subtraction will be negligible.

A.2. Target Acquisition

A.2.1. Astrometry of α Cen and ϵ Mus

The α Cen AB system has a parallax of 750 mas and an annual proper motion of $(-3640, +700)$ mas yr^{-1}, which corresponds to a mean motion of $\sim$10 mas/day. The description of the procedures leading to the detailed ephemeris used for the observations are provided in Akeson et al. (2021). As described in Appendix B, the ephemeris is based on a combination of absolute astrometry from Hipparcos and ALMA. Radial velocity observations of both α Cen A and α Cen B help determine the motions of α Cen AB in their 80 year orbit. The ephemeris was calculated on an hour-by-hour basis, including the effects of parallax as observed from the vantage point of JWST's L2 orbit (Figure A1). The location of JWST at L2, an additional 1.5 million km from Earth, increases the parallactic effect by 1% or 7.5 mas, but in a non-intuitive manner due to JWST's motion at L2 (Figure A2). This effect is not negligible compared to the $\theta_{LD} = 8.5$ mas angular diameter of α Cen A (Kervella et al. 2017) and the centering accuracy requirement ($\sim$10 mas) for best performance behind the MIRI coronagraphic mask (Boccaletti et al. 2022).

The precise location of JWST at the epoch of these observations was obtained from the JPL Horizons website[9]. The combination of visible data and two epochs of ALMA data (2018/2019 from Akeson et al. 2021) and the 2023 ALMA DDT observations (described in Appendix B.1) for α Cen AB yields a precision of $\sim$2 mas in the predicted position of α Cen A (Figure A2 and Table A1). Taking into account the astrometric precision of the Gaia stars and of α Cen itself, we estimate that the overall astrometric precision of the blind offset between the offset stars and the two targets, ϵ Mus
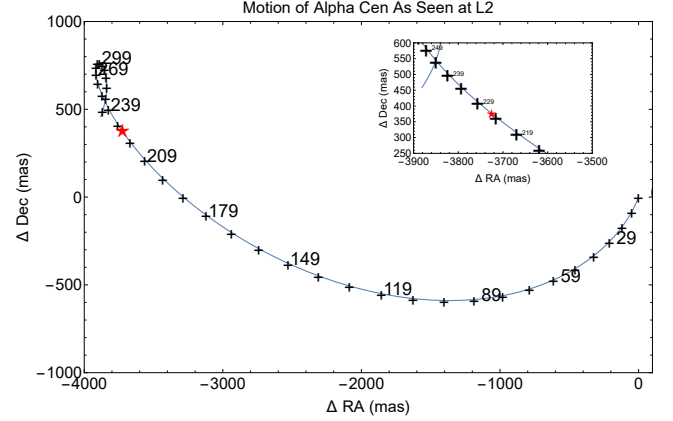
Figure A1. The change in the position of α Cen A relative to 2024-Jan-1 ($\Delta\alpha = 0$, $\Delta\delta = 0$) computed using proper motion and parallax as seen from JWST's L2 vantage point. Markers denote 10-day intervals and days of the year. As a reference, the red star denotes the date of the August 2024 JWST observations (first epoch). The inset plot zooms-in near the August 2024 observation date with markers spaced in 5-day intervals. Details of the astrometry for α Cen are given in Appendix B and in Akeson et al. (2021).

and α Cen A, will be $\sim$2.5 mas (1σ), to which must be added the $\sim$5–7 mas (1σ, one axis) offsetting precision of JWST itself[10]. Astrometry for ϵ Mus, its associated Gaia offset star, and α Cen A's associated Gaia offset star was obtained from the Gaia DR3 catalog (Table A2). The effects of the proper motion and parallax values were taken into account but were relatively minor compared to those for α Cen A.

In planning the observational sequences in APT, we specified the exact V3 rotation angles (with a precision of 0.001°) for each observation and used that information to derive the shift from the Gaia offset star to either α Cen A or ϵ Mus in instrument (x, y) coordinates. For α Cen A, these calculations used the position of α Cen A

---

[9] https://ssd.jpl.nasa.gov/horizons/app.html/

[10] https://jwst-docs.stsci.edu/jwst-observatory-characteristics/jwst-pointing-performance

Table A2. Gaia Astrometry for ε Mus and Offset Stars

| Star	Gaia ID	R.A.	Decl.	μR.A.	μDecl.	Parallax	Total Uncertainty[a]	F_ν (F1000W)[b]
		(deg, 2016.0)	(deg, 2016.0)	(mas yr^{-1})	(mas yr^{-1})	(mas)	(mas)	(μJy)
ε Mus	5859405805013401984	184.3887799	−67.960909	−230.60 ± 0.19	−26.21 ± 0.26	9.99 ± 0.20	2.68	$\cdots$
ε Mus TA[c] (G9)	5859405804986931200	184.3941452	−67.953630	−7.11 ± 0.02	0.43 ± 0.02	0.14 ± 0.02	0.21	13450
α Cen TA[d] (G0)	5877725249280411392	219.8776270	−60.828383	−1.79 ± 0.11	−1.01 ± 0.11	0.32 ± 0.09	1.28	1350
α Cen TA[e] (G5)	5877725146201190144	219.8800796	−60.8445635	−2.71 ± 0.17	−2.63 ± 0.28	0.001 ± 0.230	0.23	580

[a] Combined uncertainty from parallax and proper motion between 2016.0 and 2024.3.

[b] Flux density measured in June 2023 test images.

[c] Offset star used for target acquisition (TA) of ε Mus in all three epochs.

[d] Offset star used for target acquisition (TA) of α Cen A in August 2024 and February 2025.

[e] Offset star used for target acquisition (TA) of α Cen A in April 2025.

Table A3. Log of Successful JWST/MIRI Observations of α Cen A

PID-Obs. #	Target	# Dither	Science Time (hr)	Start Time (UTC)	Observation Mid-Point (UTC)	MIRI (X,Y) Offsets[a] (arcsec)
1618-11	α Cen Snapshot (F1000W)[b]	4	0.19	06/19/2023 10:00	$\cdots$	$\cdots$
1618-50	ε Mus Snapshot (F1000W)[b]	4	0.19	06/19/2023 10:00	$\cdots$	$\cdots$
1618-61	ε Mus Snapshot (F1550C)	1	0.04	07/07/2024 22:31	$\cdots$	$\cdots$
1618-62	α Cen Snapshot (F1550C)	1	0.04	07/08/2024 00:29	$\cdots$	$\cdots$
1618-63	ε Mus Background (F1550C)	1	0.04	07/08/2024 02:21	$\cdots$	$\cdots$
1618-64	α Cen Background (F1550C)	1	0.04	07/08/2024 02:52	$\cdots$	$\cdots$
1618-52	ε Mus Visit 1 (V3=135.0°)	9	7.19	08/11/2024 13:00	08/11/2024 17:04	(−47.7588, −5.2736)
1618-53	ε Mus Visit 1 Background	1	0.80	08/11/2024 21:16	$\cdots$	$\cdots$
1618-56	Alpha Cen Roll 2 (V3=112.7°)	1	2.50	08/12/2024 04:56	8/12/2024 06:32	(32.7863, 42.8539)
1618-57	Alpha Cen Visit 2 Background	1	2.50	08/12/2024 08:09	$\cdots$	$\cdots$
1618-65	ε Mus at α Cen B (V3=135°)	1	0.80	08/12/2024 17:11	08/12/2024 18:48	(−39.372, −8.104)
6797-01	ε Mus Visit 1 (V3=133.0°)	9	7.19	02/20/2025 01:00	02/20/2025 04:57	(46.9405, −9.7562)
6797-02	ε Mus Visit 1 Background	1	0.80	02/20/2025 09:04	$\cdots$	$\cdots$
6797-03	ε Mus at α Cen B	1	0.80	02/20/2025 10:13	02/20/2025 11:42	(38.4623, −7.294)
6797-06	α Cen Roll 2 (V3=294.5°)	1	2.50	02/20/2025 19:51	02/20/2025 21:20	(−38.7111, −38.6047)
6797-07	α Cen Roll 2 Background	1	2.50	02/20/2025 23:10	$\cdots$	$\cdots$
6797-08	ε Mus Visit 2 (V3=133.0°)	9	7.19	02/21/2025 02:17	02/21/2025 06:15	(46.9399, −9.7563)
6797-09	ε Mus Visit 2 Background	1	0.80	02/21/2025 10:22	$\cdots$	$\cdots$
6797-10	ε Mus at α Cen B (V3=133.0°)	1	2.50	02/21/2025 11:30	02/21/2025 13:00	(38.629, 6.781)
9252-01	ε Mus Visit 1 (V3=38.0°)	9	7.19	04/25/2025 01:00	04/25/2025 04:57	(10.96213, −46.62994)
9252-02	ε Mus Visit 1 Background	1	0.80	04/25/2025 09:04	$\cdots$	$\cdots$
9252-03	ε Mus at α Cen B	1	0.80	04/25/2025 10:13	04/25/2025 11:42	(8.01166, −38.20160)
9252-04	α Cen Roll 1 (V3=346°)	1	2.50	04/25/2025 13:35	04/25/2025 15:04	(−50.83941, −54.82857)
9252-05	α Cen Roll 1 Background	1	2.50	04/25/2025 16:53	$\cdots$	$\cdots$
9252-06	α Cen Roll 2 (V3=356°)	1	2.50	04/25/2025 19:51	04/25/2025 21:20	(−59.593412, −45.16806)
9252-07	α Cen Roll 2 Background	1	2.50	04/25/2025 23:10	$\cdots$	$\cdots$
9252-08	ε Mus Visit 2 (V3=38.0°)	9	7.19	04/26/2025 02:17	04/26/2025 06:15	(10.96213, −46.62994)
9252-09	ε Mus Visit 2 Background	1	0.80	04/26/2025 10:22	$\cdots$	$\cdots$
9252-10	ε Mus at α Cen B (V3=38.0°)	1	2.50	04/26/2025 11:30	04/26/2025 13:00	(9.51997, −37.81736)

[a] Offsets from the Gaia star to the target star were calculated based on the epoch positions using the STScI software pysiaf.

[b] The F1000W broadband image was obtained with FASTR1 using 60 groups.

Note—All F1550C coronagraphic data was obtained with FASTR1 using 30 groups with 400 integrations for ε Mus (behind the 4QPM) and 1250 integrations for α Cen A (behind the 4QPM) and ε Mus at the off-axis position of α Cen B. Observations 1618-1 to 1618-8 were obtained on 07/26/2023 and 07/27/2023 but failed due to either a guide star issues or incorrect offsets from the Gaia stars. Observations 1618-54 and 1618-58 in August 2024 and 6797-04 in February 2025 failed due to guide star issues.
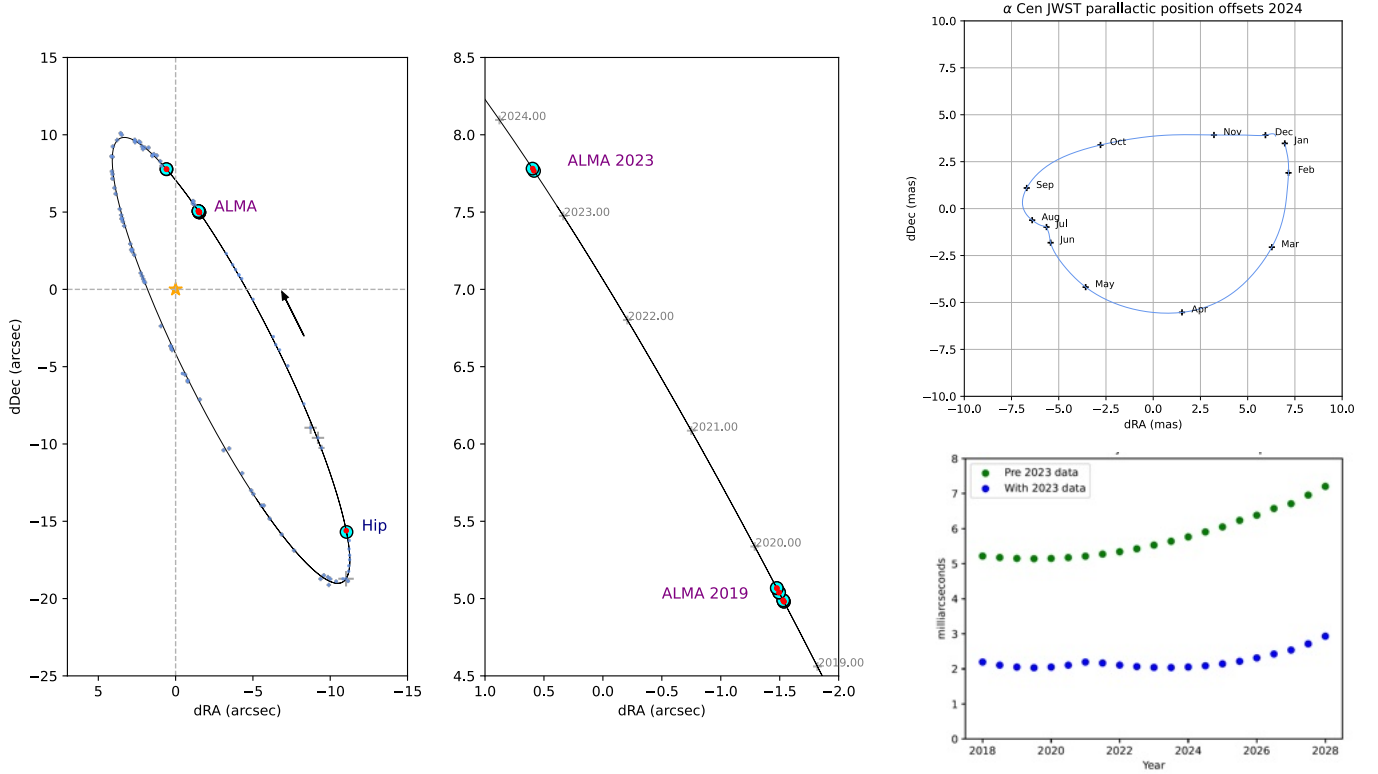
Figure A2. *Left:* Orbit of α Cen B relative to α Cen A showing one epoch of Hipparcos and two epochs of ALMA data. *Center:* zoom-in showing the ALMA data. *Top right:* The difference between the parallax effect as seen from Earth and from JWST at L2. *Bottom right:* The uncertainty in position of α Cen as a function of year before and after the addition of the new 2023 ALMA observations.

(including proper motion, parallax and other smaller effects; Akeson et al. 2021) at the expected midpoint of the observation based on a detailed timeline of each observation (Table A3). The small amount of smearing during the 2.8 hr duration of each α Cen A observation (<2 mas) was deemed acceptable compared to the complexity of designating α Cen A as a moving target. The conversion of the offset in $(\Delta\alpha, \Delta\delta)$ to instrument (x, y) was calculated for the exact epoch of observation and desired V3 angle using a model of the MIRI focal plane using STScI's `pysiaf` routine[11].

A.2.2. *Offset Star Selection and Validation*

The offset stars used for Target Acquisition were drawn from the Gaia DR3 catalog and had to have a mid-IR brightness suitable for easy measurement in a short TA observation. A preliminary search of DR3 revealed 92 targets within $60''$ of α Cen A and 24 within $30''$ of ϵ Mus. Cuts in magnitude ($G < 16$ mag) and the requirement that each star have a quoted parallax and proper motion measurement reduced the number to a handful for each source. However, the proximity of both

α Cen and ϵ Mus to the Galactic Plane ($b = -0.67°$ and $-5.30°$, respectively) means that the effects of extinction can make predictions of mid-IR brightness highly uncertain. For this reason, we scheduled test observations of both α Cen and ϵ Mus in the MIRI TA filter (F1000W) without any associated coronagraphic observations. These were executed in June 2023. Figure 1 shows images of α Cen and ϵ Mus. Simulations using `STPSF` were developed to assess the influence of the bright target stars (α Cen A, α Cen B, and ϵ Mus) to ensure that diffraction effects would not affect the detectability of the much fainter Gaia stars in the TA procedure. The star denoted G0 was suitable for both of the V3 roll angles selected for August 2024 and February 2025 (Table A2). The star denoted G5 was used for April 2025. A single star (G9) was suitable for use with ϵ Mus at its V3 angle of observation in all three epochs.

A.3. *Minimizing Effects of Telescope Slews*

The ability to detect faint companions is dominated by the stability of the wavefront of the JWST telescope and the accurate placement of the star behind the coronagraphic mask. Pre-launch expectations were that there would be slow-varying wavefront error (WFE)

---

[11] https://github.com/spacetelescope/pysiaf
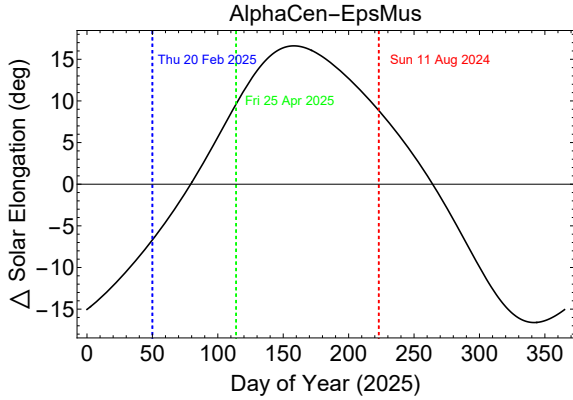
Figure A3. Change in the solar elongation angle between α Cen and ϵ Mus as a function of the day of year. The red, blue, and green dashed vertical lines correspond to the observation dates in August 2024, February 2025, and April 2025 (respectively).

drifts $\sim$10 nm depending on changes in solar elongation (and thus in the telescope's thermal balance) and due to stresses from internal structures such as the "frill" surrounding the primary mirror (Perrin et al. 2018). On-orbit performance proved to be significantly better than pre-launch estimates, particularly as the telescope assembly continued to stabilize thermally, with drifts as low as $\sim$2–5 nm as measured using semi-daily WFE monitoring observations (Rigby et al. 2023; Lajoie et al. 2023). One factor in selecting the requested observing window was minimizing the change in solar elongation angle between α Cen and ϵ Mus. The final scheduled dates in August 2024, February 2025, and April 2025 resulted in changes in the absolute value of solar angle $\lesssim 10°$ (Figure A3). To mitigate further the effects of wavefront drift, we bracketed observations of α Cen with observations of ϵ Mus. This choice provided redundancy against any failure during guide star and target acquisition by the telescope and thus would still leave one valid PSF reference star observation. Indeed, this proved to be important for the August 2024 observations where one ϵ Mus reference observation failed.

A.4. *Mitigating the Effects of α Cen B*

We initially considered strategies either using α Cen B as a reference star for α Cen A or placing α Cen B along the quadrant boundaries of the 4QPM to suppress its starlight. Both strategies had significant disadvantages. In the former case, the brighter star α Cen A would be unocculted on the detector in the reference images. In the latter case, very few opportunities were available to schedule observations in the desired configuration. Furthermore, small errors in the position of α Cen B along

the boundaries would lead to substantial stellar leakage and changes in the PSF. Our pre-launch simulations and current data analysis demonstrated that the influence of α Cen B at $7''$–$9''$ separation is sufficiently large in the $1''$–$2''$ region around α Cen A that it is necessary to subtract the image obtained by placing ϵ Mus, unocculted but through the F1550C mask, at the same offset of α Cen B relative to α Cen A to provide an off-axis PSF reference. Analysis with the test observations obtained in July 2024 showed that the use of STPSF models was inadequate to remove speckles from α Cen B at the required level.

A.5. *Mitigation of MIRI Background: The "Glow Sticks"*

Following practice recommended by STScI to mitigate the effects of the "Glow Stick" phenomenon (excess telescope background scattered off of telescope structure; Boccaletti et al. 2022; Carter et al. 2023), we included MIRI background observations in exactly the same detector and instrument setup as the on-target observations for both ϵ Mus and α Cen. These background observations were placed in positions which appeared relatively blank in Spitzer or WISE images. Each background field was observed twice for each object (Table A3) with $5''$ shifts in the center position to help mitigate the effects of sources in the fields.

B. ASTROMETRY OF THE α CEN SYSTEM

Determining the astrometric properties of the α Cen system is complex due to the proximity of α Cen to Earth and the orbits of the two stars around their common center of mass. High precision visible light observations are scarce due to the brightness of the two stars relative to much fainter reference stars. Akeson et al. (2021) made millimeter-wavelength observations of α Cen AB using the ALMA array. At these wavelengths, the two stars are bright enough to yield high SNR data with milli-arcsec precision in $\sim$ an hour of observing time with absolute positions on the ICRF reference frame. The ALMA observations are described in §B.1 and the astrometric information used for the JWST observations in §B.2.

B.1. *New ALMA Astrometry of α Cen AB*

The positions of α Cen A and α Cen B were observed with ALMA between 2018 Oct 14 and 2019 Aug 26 using about 40 25-m antennas as described in detail in Akeson et al. (2021) and summarized here. The average observing frequency was 343.5 GHz, but the ALMA configurations varied and produced a resolution of 140, 33, 28, 62, and 62 mas for the five observing blocks. Each

Table B1. New ALMA Astrometry

Date	Start Time	Star	R.A.	Decl.
	(UT hours)			
01 June 2023	02:35	A	$219.864944115°$ (±3 mas)	$-60.848591790°$ (±3 mas)
		B	$219.865261605°$ (±4 mas)	$-60.846446520°$ (±4 mas)
		A–B	$-0.''5935 \pm 0.''0004$	$-7.''6756 \pm 0.''0005$
17 June 2023	01:55	A	$219.850279410°$ (±1 mas)	$-60.831926083°$ (±1 mas)
		B	$219.850610280°$ (±1 mas)	$-60.829773243°$ (±1 mas)
		A–B	$-0.''5806 \pm 0.''0005$	$-7.''7502 \pm 0.''0005$
26 June 2023	00:59	A	$219.850180635°$ (±0.8 mas)	$-60.831902697°$ (±1.1 mas)
		B	$219.850518885°$ (±1.2 mas)	$-60.829745590°$ (±1.2 mas)
		A–B	$-0.''5715 \pm 0.''0020$	$-7.''7234 \pm 0.''0020$

block was about 80 min long and consisted of about 120 scans of which 15% included calibration sources. The pointing center of each experiment was located near the expected barycenter of the A and B stars to minimize errors caused by small antenna pointing offsets. The α Cen AB positions were determined using the phase referencing technique with the nearby quasar, J1452-6502, with an ICRF position accuracy <0.5 mas. This uncertainty produced the main limit to the absolute radio position of the AB system. However, the separation of the A and B stars do not depend on the quasar position accuracy and some of the atmospheric position jitter between the A and B stars also canceled. Further details of the reduction, imaging and multi-calibrator checks to the astrometric accuracy are given in Akeson et al. (2021).

New observations were obtained through an accepted ALMA DDT proposal on 2023 June 1, 17 and 26 (DDT proposal 2022.A.00017.S). The data were taken in Band 7 (343.5 GHz) with the correlator configured for maximum broadband sensitivity. The 2023 positions are listed in Table B1 and were derived from pipeline-processed data using additional analysis to determine the internal position uncertainties. Due to the large proper motion of α Cen, roughly 10 mas/day on average, the phase center tracking has a significant impact on the measured positions. For the 2023 June 1 observations, the α Cen A position was tracked with time, while for the 2023 June 17 and 26 observations, the phase center was located near α Cen A, but was not tracked with time.

The main improvement from the previous ALMA observations (Akeson et al. 2021) is the measurement of internal position errors. These were estimated by splitting each 50-min experiment into three independent parts and then determining the mean stellar position and the error from the scatter among the three parts. The slight stellar motion during an hour observation (0.4 mas) is much less than that caused by the typical temporal "atmospheric" variations. For the 2023 June 17 and 26 observations, where the phase center was located near α Cen A, but was not tracked with time, the α Cen A and α Cen B 1-sigma position errors are about 1.5 mas. For the 2023 June 1 observation, during which the α Cen A position was phased tracked, the location of the absolute frame of the images is uncertain, resulting in a larger absolute position error estimate (Table B1).

The absolute star positions in the DDT observations are tied to the phase calibrator (J1408-5712) whose absolute position is measured by global VLBI observations. Its absolute position has an uncertainty of about 1.5 mas which is, unfortunately, relatively large for an ICRF source since it has not been observed very often. The calibrator is located only 5.4° away from α Cen and is the closest of the brighter available calibrators. If the J1408-5712 position error and the α Cen A internal position errors are combined, then the ICRF absolute position errors should be no larger than 2 mas in R.A. and in Decl.

The separation of α Cen A and α Cen B was also obtained for these observations, again by splitting up each 50-min experiment into three parts. The estimated separation error is less than 1 mas for the 2023 June 17 and 26 observations because much of the error that affect the absolute position of A and B cancels when calculating the stellar position difference. The accuracy is mostly signal-to-noise limited. Since the A–B separation for the 2023 June 1 observation does not depend on the somewhat uncertain definition of the absolute coordi-

Table B2. Astrometry of α Cen A and α Cen B (2024–2027)

Julian Year	Time	R.A. (α Cen A)	Decl. (α Cen A)	R.A. (α Cen B)	Decl. (α Cen B)	ρ(A→B)	θ(A→B)
		(J2000, deg)	(J2000, deg)	(J2000, deg)	(J2000, deg)	(arcsec)	(deg, North = 0)
2024.0000000	2024-01-01T12:00:00.000	219.84969992	−60.83174299	219.85019709	−60.82949888	8.1258	6.1630
2024.0027379	2024-01-02T12:00:00.000	219.84969758	−60.83174528	219.85019558	−60.82950072	8.1275	6.1721
2024.0054757	2024-01-03T12:00:00.000	219.84969512	−60.83174758	219.85019396	−60.82950258	8.1293	6.1812
2024.0082136	2024-01-04T12:00:00.000	219.84969256	−60.83174989	219.85019224	−60.82950444	8.1310	6.1903
2024.0109514	2024-01-05T12:00:00.000	219.84968989	−60.83175221	219.85019041	−60.82950632	8.1328	6.1994

NOTE—The coordinates are apparent coordinates from the location of JWST. The astrometry is available at 10.5281/zenodo.16280658.

nate grid, its accuracy is only a bit larger than the two later observations.

B.2. *Astrometry of α Cen A, α Cen B and α Cen AB*

The analysis method for determining the astrometric properties of the α Cen AB system using the combined visible and ALMA data is described in Akeson et al. (2021). The updated orbit is visualized in Figure A2. Accurate knowledge of the position of α Cen A depends on accounting for the location of JWST at L2. The differences in the parallactic motion between the two observing sites, Earth and L2 is $\sim \pm 5$ mas (Figure A2). Finally, we note that the addition of the ALMA DDT observations reduced the uncertainty in the positions of α Cen A from $\sim$5–6 mas to $\sim$2 mas through 2028 (Figure A2). A detailed analysis of the orbit of α Cen AB, including all ALMA epochs and new HARPS radial velocity data will be presented in a forthcoming paper (Kervella et al., in prep).

Table B2 lists the position of α Cen A and α Cen B as seen from JWST's location (which is obtained from the HORIZONS database[12]) and lists the relative positions of α Cen A and α Cen B, which were used in positioning the reference star ε Mus at the position of α Cen B to mitigate the speckles from the unocculted star. The first few entries of the full ephemeris are displayed and the complete table is available in electronic form at 10.5281/zenodo.16280658.

REFERENCES

Akeson, R., Beichman, C., Kervella, P., et al. 2021, AJ, 162, 14. doi:10.3847/1538-3881/abfaff

Astropy Collaboration, Price-Whelan, A. M., Lim, P. L., et al. 2022, ApJ, 935, 167

Batalha, N. E., Marley, M. S., Lewis, N. K., and Fortney, J. J. 2019 ApJ, 878, 1, 70. doi:10.3847/1538-4357/ab1b51

Bayo, A., Rodrigo, C., Barrado Y Navascués, D., et al. 2008, A&A, 492, 277. doi:10.1051/0004-6361:200810395

Beichman, C. A., Bryden, G., Rieke, G. H., et al. 2005, ApJ, 622, 2, 1160. doi:10.1086/428115

Beichman, C., Ygouf, M., Llop Sayson, J., et al. 2020, PASP, 132, 015002

Beiler, S. A., Mukherjee, S., Cushing, M. C., et al. 2024, ApJ, 973, 1, 60. doi:10.3847/1538-4357/ad6759

Bendek, E. A., Belikov, R., Sirbu, D., et al. 2021, Proc. SPIE, 11823, 1182311. doi:10.1117/12.2594992

Birkby, J. & Parker, L. 2024, AAS/Division for Extreme Solar Systems Abstracts, 56, 503.01

Blunt, S., Nielsen, E. L., De Rosa, R. J., et al. 2017, AJ, 153, 229. doi:10.3847/1538-3881/aa6930

Blunt, S., Wang, J. J., Angelo, I., et al. 2020, AJ, 159, 89. doi:10.3847/1538-3881/ab6663

Boccaletti, A., Lagage, P.-O., Baudoz, P., et al. 2015, PASP, 127, 633

Boccaletti, A., Cossou, C., Baudoz, P., et al. 2022, A&A, 667, A165. doi:10.1051/0004-6361/202244578

Brooke, T. Y. *"Main Belt Asteroids in Spitzer Observations"*, 2003, https://irsa.ipac.caltech.edu/\data/SPITZER/docs/files/spitzer/asteroid_memo.pdf

Buser, R. & Kurucz, R. L. 1992, A&A, 264, 557

Bushouse, H., Eisenhamer, J., Dencheva, N., et al. 2022, JWST Calibration Pipeline, Zenodo, doi:10.5281/ZENODO.7038885. https://zenodo.org/record/7038885

Brandt, T. D. 2024, PASP, Optimal Fitting and Debiasing for Detectors Read Out Up-the-Ramp, 136, 4, 045004. doi:10.1088/1538-3873/ad38d9

[12] https://ssd.jpl.nasa.gov/horizons/app.html/

Butler R. P., Bedding T. R., Kjeldsen H., McCarthy C., O'Toole S. J., Tinney C. G., Marcy G. W., et al., 2004, ApJL, 600, L75. doi:10.1086/381434

Carter, A. L., Hinkley, S., Kammerer, J., et al. 2023, ApJL, 951, L20. doi:10.3847/2041-8213/acd93e

Carter, A., Kammerer, J., Leisenring, J., et al. 2025, Astrophysics Source Code Library, spaceKLIP: JWST coronagraphy data data reduction and analysis pipeline. ascl:2502.014

Castelli, F. & Kurucz, R. L. 2003, Modelling of Stellar Atmospheres, 210, A20. doi:10.48550/arXiv.astro-ph/0405087

Chauvin, G., Videla, M., Beust, H., et al. 2023, A&A, 675, A114. doi:10.1051/0004-6361/202244502

Christiansen, J. L., McElroy, D. L., Harbut, M., et al. 2025, , arXiv:2506.03299. doi:10.48550/arXiv.2506.03299

Clarke, Arthur. C. 1986 *The Songs of Distant Earth*, Del Rey Books (US), 1986, ISBN:0-345-33219-9

Coulter, D. J., Barnes, J. W., & Fortney, J. J. 2022, ApJS, Jupiter and Saturn as Spectral Analogs for Extrasolar Gas Giants and Brown Dwarfs, 263, 1, 15. doi:10.3847/1538-4365/ac886a

Cuello, N. & Sucerquia, M. 2024, Universe, 10, 2, 64. doi:10.3390/universe10020064

Crotts, K. A., Carter, A. L., Lawson, K., et al. 2025, , arXiv:2506.19932. doi:10.48550/arXiv.2506.19932

Dohnanyi, J. S. 1969, J. Geophys. Res., 74, 2531. doi:10.1029/JB074i010p02531

Ducati, J. R. 2002, VizieR Online Data Catalog

Dupuy, T. J., Kraus, A. L., Kratter, K. M., et al. 2022, MNRAS, 512, 648. doi:10.1093/mnras/stac306

Dupuy, T. J., Kratter, K. M., Kraus, A. L., et al. 2016, ApJ, 817, 80. doi:10.3847/0004-637X/817/1/80

Lester, K. V., Dupuy, T. J., Kraus, A. L., et al. 2023, AJ, 166, 166. doi:10.3847/1538-3881/acf167

Engels, D., Sherwood, W. A., Wamsteker, W., et al. 1981, A&AS, 45, 5

Ertel, S., Defrère, D., Hinz, P., et al. 2018, AJ, 155, 194

Ertel, S., Defrère, D., Hinz, P., et al. 2020, AJ, 159, 177

Evans, E. L., Dupuy, T. J., Sullivan, K., et al. 2024, MNRAS, 534, 575. doi:10.1093/mnras/stae2095

Farihi, J., Su, K. Y. L., Melis, C., et al. 2025, ApJL, Subtle and Spectacular: Diverse White Dwarf Debris Disks Revealed by JWST, 981, 1, L5. doi:10.3847/2041-8213/adae88

Fegley, B. & Prinn, R. G. 1985, ApJ, Equilibrium and nonequilibrium chemistry of Saturn's atmosphere - Implications for the observability of PH3, N2, CO, and GeH4., 299, 1067. doi:10.1086/163775

Feng, T. 2024, arXiv:2406.19177. doi:10.48550/arXiv.2406.19177

Feroz, F., Hobson, M. P., & Bridges, M. 2009, MNRAS, 398, 4, 1601. doi:10.1111/j.1365-2966.2009.14548.x

Foreman-Mackey, D., Hogg, D. W., Lang, D., et al. 2013, PASP, 125, 925, 306. doi:10.1086/670067

Gaia Collaboration, Prusti, T., de Bruijne, J. H. J., et al. 2016, A&A, 595, A1. doi:10.1051/0004-6361/201629272

Harris, C. R., Millman, K. J., van der Walt, S. J., et al. 2020, Nature, 585, 7825, 357. doi:10.1038/s41586-020-2649-2

Heppenheimer, T. A. 1978, A&A, 65, 421

Huang, X. & Ji, J. 2022, AJ, 164, 5, 177. doi:10.3847/1538-3881/ac8f4c

Hunter, J. D. 2007, Computing in Science and Engineering, 9, 3, 90. doi:10.1109/MCSE.2007.55

Innanen, K. A., Zheng, J. Q., Mikkola, S., et al. 1997, AJ, 113, 1915. doi:10.1086/118405

Ito, T. & Ohtsuka, K. 2020, European Planetary Science Congress, EPSC2020-269. doi:10.5194/epsc2020-269

Johnson, R. G. & McClure, B. T. 1976, Quaternary Research, A model for Northern Hemisphere continental ice sheet variation, 6, 3, 325. doi:10.1016/0033-5894(67)90001-4

Kammerer, J., Girard, J., Carter, A. L., et al. 2022, Proc. SPIE, 12180, 121803N. doi:10.1117/12.2628865

Kelsall, T., Weiland, J. L., Franz, B. A., et al. 1998, ApJ, The COBE Diffuse Infrared Background Experiment Search for the Cosmic Infrared Background. II. Model of the Interplanetary Dust Cloud, 508, 1, 44. doi:10.1086/306380

Kennedy, G. M., Wyatt, M. C., Su, K. Y. L., et al. 2011, MNRAS, 417, 2281.

Kennedy, G. M., & Wyatt, M. C. 2013, MNRAS, 433, 2334

Kennedy, G. M., Matrà, L., Marmier, M., et al. 2015, MNRAS, Kuiper belt structure around nearby super-Earth host stars, 449, 3, 3121. doi:10.1093/mnras/stv511

Kervella, P., Mignard, F., Mérand, A., & Thévenin, F. 2016, A&A, 594, A107

Kervella, P., Bigot, L., Gallenne, A., et al. 2017, A&A, 597, A137

Kozai, Y. 1962, AJ, 67, 591. doi:10.1086/108790

Kraus, A. L., Ireland, M. J., Huber, D., Mann, A. W., & Dupuy, T. J. 2016, AJ, 152, 8

Kuchner, M. 2012, Astrophysics Source Code Library, "ZODIPIC: Zodiacal Cloud Image Synthesis", ascl:1202.002

Lacy, B. & Burrows, A. 2023, ApJ, Self-consistent Models of Y Dwarf Atmospheres with Water Clouds and Disequilibrium Chemistry, 950, 1, 8. doi:10.3847/1538-4357/acc8cb

Lajoie, C.-P., Lallo, M., Meléndez, M., et al. 2023, Technical Report JWST-STScI-008497. doi:10.48550/arXiv.2307.11179

Leggett, S. K., Saumon, D., Marley, M. S., et al. 2007, ApJ, 3.6-7.9 μm Photometry of L and T Dwarfs and the Prevalence of Vertical Mixing in their Atmospheres, 655, 2, 1079. doi:10.1086/510014

Leggett, S. K., Tremblin, P., Phillips, M. W., et al. 2021, ApJ, Measuring and Replicating the 1-20 μm Energy Distributions of the Coldest Brown Dwarfs: Rotating, Turbulent, and Nonadiabatic Atmospheres, 918, 1, 11. doi:10.3847/1538-4357/ac0cfe

Leggett, S. K. & Tremblin, P. 2023, ApJ, The First Y Dwarf Data from JWST Show that Dynamic and Diabatic Processes Regulate Cold Brown Dwarf Atmospheres, 959, 2, 86. doi:10.3847/1538-4357/acfdad

Leggett, S. K. & Tremblin, P. 2024, Research Notes of the American Astronomical Society, James Webb Space Telescope Spectra of Cold Brown Dwarfs are Well-reproduced by Phosphine-free, Diabatic, ATMO2020++ Models, 8, 1, 13. doi:10.3847/2515-5172/ad1b61

Leisenring, J. 2024, ApJ, in prep

Li,L., Jiang, X., West, R. A. it Nature Comm., 3709, https://doi.org/10.1038/s41467-018-06107-2

Lidov, M. L. 1962, Planet. Space Sci., 9, 10, 719. doi:10.1016/0032-0633(62)90129-0

Lightsey, P. A., Knight, J. S., Barto, A., et al. 2018, Proceedings Volume 10698, Space Telescopes and Instrumentation 2018: Optical, Infrared, and Millimeter Wave; 1069804 (2018) https://doi.org/10.1117/12.2312276

Lissauer, J. J., Marcy, G. W., Bryson, S. T., et al. 2014, ApJ, 784, 44

Luhman, K. L., Tremblin, P., Alves de Oliveira, C., et al. 2024, AJ, JWST/NIRSpec Observations of the Coldest Known Brown Dwarf, 167, 1, 5. doi:10.3847/1538-3881/ad0b72

Marley, M. S., Saumon, D., Visscher, C., et al. 2021, ApJ, The Sonora Brown Dwarf Atmosphere and Evolution Models. I. Model Description and Application to Cloudless Atmospheres in Rainout Chemical Equilibrium, 920, 2, 85. doi:10.3847/1538-4357/ac141d

Mawet, D., Milli, J., Wahhaj, Z., et al. 2014, ApJ, 792, 2, 97. doi:10.1088/0004-637X/792/2/97

Meisner, A. M., Leggett, S. K., Logsdon, S. E., et al. 2023, AJ, Exploring the Extremes: Characterizing a New Population of Old and Cold Brown Dwarfs, 166, 2, 57. doi:10.3847/1538-3881/acdb68

Moe, M. & Kratter, K. M. 2021, MNRAS, 507, 3593. doi:10.1093/mnras/stab2328

Morley, C. V., Marley, M. S., Fortney, J. J., et al. 2014, ApJ, Water Clouds in Y Dwarfs and Exoplanets, 787, 1, 78. doi:10.1088/0004-637X/787/1/78

Mukherjee, S., Batalha, N. E., Fortney, J. J., and Marley, M. S., 2023 ApJ, 942, 2, 71 doi:10.3847/1538-4357/ac9f48

Mukherjee, S., Fortney, J. J., Morley, C. V., et al. 2024, ApJ, 963, 1, 73. doi:10.3847/1538-4357/ad18c2

Müller, S., Baron, J., Helled, R., et al. 2024, A&A, 686, A296. doi:10.1051/0004-6361/202348690

Murakami, H., Baba, H., Barthel, P., et al. 2007, PASJ, 59, S369. doi:10.1093/pasj/59.sp2.S369

Naoz, S. 2016, ARA&A, 54, 441. doi:10.1146/annurev-astro-081915-023315

Noll, K. S., Geballe, T. R., & Marley, M. S. 1997, ApJL, Detection of Abundant Carbon Monoxide in the Brown Dwarf Gliese 229B, 489, 1, L87. doi:10.1086/310954

Olnon, F. M., Raimond, E., Neugebauer, G., et al. 1986, A&A(S), 65, 607

Peale, S. J. & Cassen, P. 1978, Icarus, Contribution of tidal dissipation to lunar thermal history, 36, 2, 245. doi:10.1016/0019-1035(78)90109-4

Perrin, M. D., Sivaramakrishnan, A., Lajoie, C.-P., et al. 2014, in Society of Photo-Optical Instrumentation Engineers (SPIE) Conference Series, Vol. 9143, Space Telescopes and Instrumentation 2014: Optical, Infrared, and Millimeter Wave, ed. J. Oschmann, Jacobus M., M. Clampin, G. G. Fazio, & H. A. MacEwen, 91433X

Perrin, M. D., Pueyo, L., Van Gorkom, K., et al. 2018, Proceedings Volume 10698, Space Telescopes and Instrumentation 2018: Optical, Infrared, and Millimeter Wave; 1069809 (2018) https://doi.org/10.1117/12.2313552

Phillips, M. W., Tremblin, P., Baraffe, I., et al. 2020, A&A, A new set of atmosphere and evolution models for cool T-Y brown dwarfs and giant exoplanets, 637, A38. doi:10.1051/0004-6361/201937381

Planck Collaboration, Ade, P. A. R., Aghanim, N., et al. 2016, A&A, 586, A132. doi:10.1051/0004-6361/201424945

Polletta, M., Tajer, M., Maraschi, L., et al. 2007, ApJ, 663, 81. doi:10.1086/518113

Quarles, B. & Lissauer, J. J. 2016, AJ, 151, 111

Quarles, B., & Lissauer, J. J. 2018, AJ, 155, 130

Quarles, B., Lissauer, J. J., & Kaib, N. 2018, AJ, 155, 64

Quintana, E. V., Lissauer, J. J., Chambers, J. E., & Duncan, M. 2002, ApJ, 576, 2. doi:10.1086/341808

Quirrenbach, A. 2022, Research Notes AAS, 6, 3, 56. doi:10.3847/2515-5172/ac5f0d

Rafikov, R. R., & Silsbee, K. 2014, ApJ, 798, 70. doi:10.1088/0004-637X/798/2/70

Rieke, G. & Gautier, N. 2004, Spitzer Proposal, 52

Rigby, J., Perrin, M., McElwain, M., et al. 2023, PASP, 135, 048001. doi:10.1088/1538-3873/acb293

Rein, H. and S.-F. Liu 2012, A&A537 A128.

Rein, H., D. Tamayo, and G. Brown 2019, MNRAS489 4632.

Rieke, G. H., Ressler, M. E., Morrison, J. E., et al. 2015, PASP, 127, 665.doi:10.1086/682252

Sanghi, A., Beichman, C., Mawet, D., et al. 2025, Research Notes of the American Astronomical Society, 9, 5, 119. doi:10.3847/2515-5172/add880

Sanghi, A, Beichman, C.A, et al. 2025, in press.

Silsbee, K., & Rafikov, R. R. 2021, A&A, 652, A104. doi:10.1051/0004-6361/202141139

Soummer, R., Pueyo, L., & Larkin, J. 2012, ApJL, 755, 2, L28. doi:10.1088/2041-8205/755/2/L28

STScI Development Team 2013, Astrophysics Source Code Library. ascl:1303.023

Rigley, J. K. & Wyatt, M. C. 2020, MNRAS, 497, 1143

Saumon, D., Marley, M. S., Cushing, M. C., et al. 2006, ApJ, Ammonia as a Tracer of Chemical Equilibrium in the T7.5 Dwarf Gliese 570D, 647, 1, 552. doi:10.1086/505419

Sommer, M., Wyatt, M., & Han, Y. 2025, MNRAS, 539, 439. doi:10.1093/mnras/staf494

Stone, M. A., Alberts, S., Rieke, G. H., et al. 2024, ApJ, 5–25 μm Galaxy Number Counts from Deep JWST Data, 972, 1, 62. doi:10.3847/1538-4357/ad6308

Su, K. Y. L., Rieke, G. H., Malhotra, R., et al. 2013, ApJ, 763, 118

Sullivan, K., Kraus, A. L., Berger, T. A., et al. 2024, AJ, 168, 129. doi:10.3847/1538-3881/ad6310

Tabur, V., Bedding, T. R., Kiss, L. L., et al. 2009, MNRAS, 400, 1945. doi:10.1111/j.1365-2966.2009.15588.x

Teplitz, V. L., Stern, S. A., Anderson, J. D., et al. 1999, ApJ, 516, 425

Thebault, P., Kral, Q., & Olofsson, J. 2021, A&A, 646, A173. doi:10.1051/0004-6361/202039582

Thebault, P., Marzari, F., & Scholl, H. 2008, MNRAS, 388, 1528. doi:10.1111/j.1365-2966.2008.13524.x

Trilling, D. E., Stansberry, J. A., Stapelfeldt, K. R., et al. 2007, ApJ, 658, 1289. doi:10.1086/511668

Tuthill, P., Bendek, E., Guyon, O., et al. 2018, Proc. SPIE, 10701, 107011J. doi:10.1117/12.2313269

Valenti, J. A. & Fischer, D. A. 2005, ApJS, 159, 141. doi:10.1086/430500

Virtanen, P., Gommers, R., Oliphant, T. E., et al. 2020, Nature Methods, 17, 261. doi:10.1038/s41592-019-0686-2

von Zeipel, H. 1910, Astronomische Nachrichten, 183, 22, 345. doi:10.1002/asna.19091832202

Wang, J. J., Ruffio, J.-B., De Rosa, R. J., et al. 2015, pyKLIP: PSF Subtraction for Exoplanets and Disks, Astrophysics Source Code Library, record ascl:1506.001.

Wiegert, J., Liseau, R., Thébault, P., et al. 2014, A&A, 563, A102. doi:10.1051/0004-6361/201321887

Wagner, K., Boehle, A., Pathak, P., et al. 2021, Nature Communications, 12, 922. doi:10.1038/s41467-021-21176-6

Wogan, N. F., Mang, J., Batalha, N. E., et al. 2025, Research Notes of the American Astronomical Society, 9, 5, 108. doi:10.3847/2515-5172/add407

Wittenmyer, R. A., Butler, R. P., Tinney, C. G., et al. 2016, ApJ, 819, 28. doi:10.3847/0004-637X/819/1/28

Wright, G. S., Wright, D., Goodson, G. B., et al. 2015, PASP, 127, 595. doi:10.1086/682253

Wyatt, M. C. 2005, A&A, The insignificance of P-R drag in detectable extrasolar planetesimal belts, 433, 3, 1007. doi:10.1051/0004-6361:20042073

Wyatt, M. C., Smith, R., Su, K. Y. L., et al. 2007, ApJ, 663, 365. doi:10.1086/518404

Wyatt, M. C., Clarke, C. J., & Booth, M. 2011, Celestial Mechanics and Dynamical Astronomy, Debris disk size distributions: steady state collisional evolution with Poynting-Robertson drag and other loss processes, 111, 1-2, 1. doi:10.1007/s10569-011-9345-3

Xuan, J. W. & Wyatt, M. C. 2020, MNRAS, 497, 2, 2096. doi:10.1093/mnras/staa2033

Yelverton, B., Kennedy, G. M., Su, K. Y. L., & Wyatt, M. C. 2019, MNRAS, 488, 3588. doi:10.1093/mnras/stz1927

Zahnle, K. J. & Marley, M. S. 2014, ApJ, 797, 1, 41. doi:10.1088/0004-637X/797/1/41

Zhang, M. & Kainulainen, J. 2022, MNRAS, 517, 5180. doi:10.1093/mnras/stac3012

Zhang, J., Wang, J., Howell, S. B., et al. 2024, AJ, 167, 89. doi:10.3847/1538-3881/ad2152

Zhao, L., Fischer, D. A., Brewer, J., et al. 2018, AJ, 155, 24